SPECIAL
Oceanic Flow–Topography Interactions
COLLECTION

Tidal Intrusion Fronts, Surface Convergence, and Mixing in an Estuary with Complex Topography

TONG BO,[a,b,c] DAVID K. RALSTON,[a] ADRIAN MIKHAIL P. GARCIA,[a,b,d] AND W. ROCKWELL GEYER[a]

[a] *Applied Ocean Physics and Engineering Department, Woods Hole Oceanographic Institution, Woods Hole, Massachusetts*
[b] *MIT–WHOI Joint Program in Oceanography/Applied Ocean Science and Engineering, Cambridge, Massachusetts*
[c] *Department of Atmospheric and Oceanic Sciences, University of California, Los Angeles, Los Angeles, California*
[d] *Exponent, Inc., Bellevue, Washington*

(Manuscript received 12 July 2023, in final form 6 November 2023, accepted 28 December 2023)

ABSTRACT: Observations from a tidal estuary show that tidal intrusion fronts occur regularly during flood tides near topographic features including constrictions and bends. A realistic model is used to study the generation of these fronts and their influence on stratification and mixing in the estuary. At the constriction, flow separation occurs on both sides of the jet flow downstream of the narrow opening, leading to sharp lateral salinity gradients and baroclinic secondary circulation. A tidal intrusion front, with a V-shaped convergence zone on the surface, is generated by the interaction between secondary circulation and the jet flow. Stratification is created at the front due to the straining of lateral salinity gradients by secondary circulation. Though stratification is expected to suppress turbulence, strong turbulent mixing is found near the surface front. The intense mixing is attributed to enhanced vertical shear due to both frontal baroclinicity and the twisting of lateral shear by secondary circulation. In the bend, flow separation occurs along the inner bank, resulting in lateral salinity gradients, secondary circulation, frontogenesis, and enhanced mixing near the front. In contrast to the V-shaped front at the constriction, an oblique linear surface convergence front occurs in the bend, which resembles a one-sided tidal intrusion front. Moreover, in addition to baroclinicity, channel curvature also affects secondary circulation, frontogenesis, and mixing in the bend. Overall in the estuary, the near-surface mixing associated with tidal intrusion fronts during flood tides is similar in magnitude to bottom boundary layer mixing that occurs primarily during ebbs.

KEYWORDS: Estuaries; Fronts; Mixing; Secondary circulation; Tides; Numerical analysis/modeling

1. Introduction

Surface fronts are ubiquitous in estuaries (e.g., Simpson and Turrell 1986; Largier 1992; O'Donnell 1993). As regions where two distinct water masses interact and generate sharp density gradients (Largier 1993), estuarine surface fronts usually have strong horizontal convergence due to baroclinicity from the frontal density gradient (Valle-Levinson et al. 2000; Giddings et al. 2012; Collignon and Stacey 2012). The convergence means these surface features are typically identifiable by accumulated foam and debris, in addition to sharp color discontinuities that are often visible (Brown et al. 1991; Largier 1992). Correspondingly, fronts have important implications for transport and aggregation of pollutants, phytoplankton, and larvae (Tyler et al. 1982; Brown et al. 1991; Wang et al. 2022).

Examples of surface fronts in estuaries include tidal intrusion fronts (Simpson and Nunes 1981), axial convergence fronts (Nunes and Simpson 1985), and plume fronts (Garvine 1974). These categories are not mutually independent—e.g., tidal intrusion fronts, which appear as denser water intrudes into a basin of buoyant water, are dynamically similar to plume fronts that form when buoyant water discharges into a region with denser water (O'Donnell 1993). Both tidal intrusion fronts and axial convergence fronts result from the differential advection of longitudinal density gradients by tidal currents (Simpson and Turrell 1986), and axial convergence fronts have been observed to originate at the apex of tidal intrusion fronts (Largier 1992). Moreover, axial convergence fronts can produce buoyancy-driven flow structures that propagate away from the generation region as plume fronts (O'Donnell 1993).

This research focuses on tidal intrusion fronts that form as seawater is advected into estuaries by flood tide currents. Tidal intrusion fronts typically exhibit a V-shaped configuration, with horizontal recirculation zones on both sides of the front and intense surface convergence along the centerline (Simpson and Nunes 1981; Largier 1992). Nevertheless, the

Supplemental information related to this paper is available at the Journals Online website: https://doi.org/10.1175/JPO-D-23-0131.s1.

Corresponding author: Tong Bo, tbo@whoi.edu

DOI: 10.1175/JPO-D-23-0131.1

mechanisms of frontogenesis and mixing investigated here apply to other surface fronts with different morphologies but similar dynamics, as will be discussed later.

Topographic complexity, e.g., channel constrictions, shallow shoals, confluences, headlands, and meanders, are often important sites for estuarine frontogenesis (e.g., Largier 1992; Giddings et al. 2012; Geyer and Ralston 2015). Complex topographic features can generate 3D flow structures that interact with the salinity field, and fronts are created as secondary circulation sharpens salinity gradients through normal or shear straining (McWilliams 2021). Constrictions and channel–shoal bathymetry can lead to strong lateral shear in tidal flows and create lateral salinity gradients through differential advection (Nunes and Simpson 1985; Lacy et al. 2003; Collignon and Stacey 2012; Li et al. 2014). The associated lateral baroclinic forcing drives secondary circulation in the channel cross section, resulting in lateral convergence near the surface, increasing lateral salinity gradients, and contributing to frontogenesis. In addition to differential advection, lateral salinity fronts may result from lateral trapping by side channels or mudflats (Valle-Levinson et al. 2000; Giddings et al. 2012; Garcia et al. 2022), with baroclinic dynamics and secondary circulation similar to differential advection. In channel bends, curvature can drive secondary circulation through the centrifugal acceleration in the lateral momentum balance (Thomson 1877; Kalkwijk and Booij 1986; Geyer 1993). The development of secondary circulation, as well as its interaction with the salinity field and influence on frontogenesis, thus depends on both centrifugal acceleration and baroclinic forcing in sinuous estuaries (Lacy and Monismith 2001; Nidzieko et al. 2009; Becherer et al. 2015; Kranenburg et al. 2019).

In addition to its influence on frontogenesis, secondary circulation associated with topographic complexity plays crucial roles in affecting stratification, vertical mixing, and horizontal dispersion. For example, secondary circulation and lateral straining of salinity gradients can increase or decrease stratification (Lacy et al. 2003; Giddings et al. 2012; Scully and Geyer 2012; Becherer et al. 2015; Bo and Ralston 2022). In a shallow estuary in the Salish Sea, Giddings et al. (2012) observed that a surface front and the associated secondary circulation led to enhanced stratification in late flood tide, thus suppressing vertical turbulent mixing. In contrast, Collignon and Stacey (2013) reported that secondary circulation was responsible for turbulence generation in late ebb tides at the channel–shoal interface in South San Francisco Bay. Similarly, in the James River, Huguenard et al. (2015) found that near-surface turbulence and mixing was related to secondary circulation during ebb tides. Secondary circulation associated with topographic complexity, e.g., channel–shoal systems and meanders, can also affect the subtidal structure of salinity and longitudinal velocity fields, thereby impacting the landward salt flux (e.g., Lerczak and Geyer 2004; Ralston and Stacey 2005; Becherer et al. 2015; Geyer et al. 2020)

In this research, we conduct a numerical modeling study of the North River estuary (Massachusetts, United States), an intermittently stratified, shallow tidal channel with complex topography (Kranenburg et al. 2019; Bo et al. 2021; Garcia et al. 2022). Surface fronts have been regularly observed during flood tides at multiple locations along the estuary, and fronts are particularly associated with topographic features like channel constrictions and bends. We investigate in detail the frontal structures and associated secondary circulation at two representative locations, a constriction and a bend. The influences of fronts and secondary circulation on stratification and turbulent mixing in the estuary are also examined. In section 2, we introduce the study site, model setup, observations, and the theoretical framework for studying secondary circulation, stratification, and mixing. Section 3 presents the results and analysis, and we discuss their implications in section 4. Section 5 presents our conclusions.

2. Methods

a. Study site

The North River estuary is a sinuous tidal channel that connects to Massachusetts Bay (Fig. 1a). The typical channel depth is around 5 m, and the width is 50–100 m. The tides in the estuary are dominantly semidiurnal, with a tidal range between 2 and 4 m (Kranenburg et al. 2019; Bo et al. 2021). The maximum tidal velocity in the estuary varies between 0.5 and 1 m s^{-1} with the neap–spring cycle. The freshwater discharge is usually less than 10 m^3 s^{-1}, corresponding to a mean velocity of <0.05 m s^{-1}, but can be up to 30 m^3 s^{-1} due to rainfall events. The salinity intrusion distance typically varies from around 8 to 14 km (Garcia et al. 2022).

Two examples of characteristic topographic features are a channel constriction at 2 km into the estuary (Fig. 1c) and a channel bend at 4 km (bend1 in Fig. 1b). In the constriction region, constructed embankments from an abandoned railroad impose lateral topographic constraints on the channel. The main opening is on the south side with a width of 40 m and depth of 10 m (Fig. 1c). A smaller, secondary opening is on the north side with a width of less than 10 m and depth less than 1 m. Landward of the constriction, the channel expands to 100–200 m wide, and a shallow shoal in the southern part of the channel has a depth of ~2 m. The channel curvature is mild near the constriction, with a radius of curvature of around 300 m. In this study, we focus on the main opening that conveys most of the tidal exchange.

In the bend at around 4 km, the channel undergoes a nearly 90° turn (bend1 in Fig. 1b) with a radius of curvature of around 100 m. The channel width is 60–80 m and is relatively uniform through the bend, and the depth is around 5 m. Other bends in the mid- and lower estuary similarly have widths of 50–100 m and radii of curvature of 50–300 m. This corresponds to curvature ratios (bend sharpness) of around 1–5, which is in the typical range for natural river and tidal meanders (Leopold and Wolman 1960; Marani et al. 2002). The bend at 4 km is selected as a representative example, but similar surface fronts and frontal dynamics occur in many other bends in the North River estuary.

b. Numerical simulations

The Regional Ocean Modeling System (ROMS) (Shchepetkin and McWilliams 2005; Haidvogel et al. 2008; Warner et al. 2008,

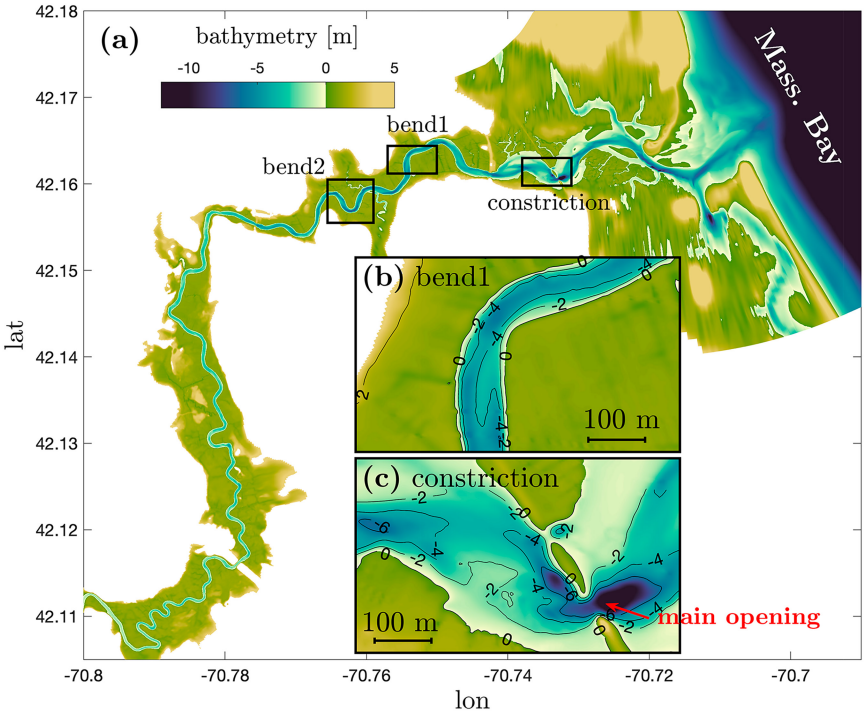

FIG. 1. (a) North River estuary model bathymetry. The constriction is located at around 2 km into the estuary. Bend1 is at around 4 km into the estuary, and this bend is selected for detailed model analysis. Bend2 is at around 5.5 km into the estuary, where drone imagery was obtained. (b) Bathymetry of the bend region (bend1). (c) Bathymetry of the constriction region.

2010) is used to simulate the North River estuary (Fig. 1a). An orthogonal curvilinear grid is built that extends from Massachusetts Bay to around 18 km into the estuary. The finest horizontal resolution is 3 m in the channel (around 10–30 grid cells across the channel) and grid spacing increases offshore and in the marsh away from the channel. A terrain-following coordinate with 16 uniformly distributed layers is used in the vertical direction. The k–ϵ closure of the generic length scale (GLS) turbulence closure scheme is used for the vertical mixing (Umlauf and Burchard 2003; Warner et al. 2005). The bottom roughness z_0 is a uniform of 0.005 m in the domain, except that z_0 is locally increased to 0.2 m in a section with large rocks on the bed located around 7 km from the mouth to better represent the decrease in tidal amplitude in that region. A third-order upwind advection scheme is used for horizontal advection. The horizontal mixing coefficient is 0.01 $m^2 s^{-1}$, and it is small enough to have no appreciable influence on the resulting velocity structure. The wetting and drying algorithm (Warner et al. 2013) is employed to simulate tidal inundation and drainage over the marsh platform and shallow shoals within the channel. The critical depth for shutting off volumetric flux from a grid cell is set to 0.02 m.

The simulations cover a 1-month period from early October to early November in 2021. Tidal fluctuations on the ocean boundaries were extracted from the ADCIRC database (Luettich et al. 1992). Subtidal fluctuations were obtained from the low-pass filtered (Butterworth filter, with a cutoff period of 33 h) water surface elevation record from the National Oceanic and Atmospheric Administration (NOAA) station at Boston (8443970). River discharge was input as a freshwater source on the western boundary based on data from the U.S. Geological Survey (USGS) gauge at Hanover (01105730) multiplied by 2.3 to account for freshwater inputs below the gauge. Wind forcing was not included in the model.

The model setup is essentially the same as that described by Bo et al. (2023) to study the hydrodynamic drag and salt intrusion in the North River. The model was evaluated in Bo et al. (2023) by comparing it with the measured tidal water levels, velocities, and salinity from long-term moorings and shipboard surveys in 2017. In this research, we focus on simulations of a 1-month period in 2021, and the model results are compared with observations in 2021 (described in the following section) for a skill assessment (Murphy 1988). The skill scores are higher than 0.95 for water level, in the range of 0.9–0.95 for velocity, and around 0.8 for salinity (Fig. 2).

c. *Field observations*

Field measurements were made in the North River estuary from September to November 2021. Four long-term moorings were deployed at around 0, 2 (near the constriction), 5, and 8 km into the estuary. At each mooring, pressure and salinity time series were measured by conductivity–temperature–depth (CTD) sensors mounted near the surface and the bed. Velocity profile data were collected at each of the three seaward mooring sites by an upward-looking Aquadopp profiler mounted on the bed. The long-term measurements of water level, salinity, and velocity were used for model assessment.

In addition, aerial drone imagery of surface fronts was obtained at multiple topographic features, including the constriction and several bends, by a DJI Phantom 4 drone. The drone imagery was used to characterize the structures of surface fronts.

d. Theoretical framework

To develop the theoretical framework for analyzing tidal intrusion fronts, stratification, and mixing, we first introduce the momentum and vorticity equations for secondary circulation with curvature [sections 2d(1) and 2d(2)]. Next, an analysis of the tendency of the gradient Richardson number is used to assess the effects of secondary circulation on water column stability [section 2d(3)]. Finally, we present the salinity variance budget to quantify the stratification, straining, and mixing associated with tidal intrusion fronts [section 2d(4)].

1) MOMENTUM EQUATIONS

The streamwise and lateral momentum equations for flow with curvature are

$$\frac{Du}{Dt} = -g\frac{\partial \eta}{\partial x} - \beta g\int_z^\eta \frac{\partial s}{\partial x}dz + \mathrm{sgn}(R)\frac{uv}{R} + \frac{\partial}{\partial z}K_v\frac{\partial u}{\partial z}, \tag{1a}$$

$$\frac{Dv}{Dt} = -g\frac{\partial \eta}{\partial y} - \beta g\int_z^\eta \frac{\partial s}{\partial y}dz - \mathrm{sgn}(R)\frac{u^2}{R} + \frac{\partial}{\partial z}K_v\frac{\partial v}{\partial z}, \tag{1b}$$

where

$$\frac{D}{Dt} = \frac{\partial}{\partial t} + u\frac{\partial}{\partial x} + v\frac{\partial}{\partial y} + w\frac{\partial}{\partial z}. \tag{2}$$

The local coordinates generally follow the channel orientation, with x, y, z being the streamwise, lateral, and vertical directions, and u, v, w being the corresponding velocity components. Coordinate $+x$ is generally eastward (ebb direction) in the study area of the North River, and $+y$ is generally northward (90° counterclockwise rotation of the ebb direction). The term η is water level and s is salinity. The term β is the haline contraction coefficient and K_v is the vertical eddy viscosity. Variable R is the radius of curvature; $\mathrm{sgn}(R) > 0$ when the $+y$ direction is toward the center of the bend, and vice versa. Note that here D/Dt is not the material derivative because this study employs curvilinear coordinates instead of Cartesian coordinates. Noninertial terms (curvature forcing terms) arise in curvilinear coordinates, i.e., the third terms on the right side of (1a) and (1b), and the noninertial term in (1b) is usually referred to as the centrifugal forcing. We use the expression D/Dt and put the noninertial terms on the right side for the convenience of the following analysis. Coriolis has been neglected as it is usually not important in small estuaries like the North River.

To study the terms responsible for secondary circulation, we subtract the depth-averaged (1b) from (1b) (e.g., Geyer 1993; Chant and Wilson 1997; Nidzieko et al. 2009) and write

$$\underbrace{\frac{\partial v}{\partial t}}_{\text{unsteady}} + \underbrace{\left(u\frac{\partial v}{\partial x} - \overline{u\frac{\partial v}{\partial x}}\right)}_{\text{advection}} = \underbrace{-\beta g\left(\int_z^\eta \frac{\partial s}{\partial y}dz - \overline{\int_z^\eta \frac{\partial s}{\partial y}dz}\right)}_{\text{BCPG}} \underbrace{-\mathrm{sgn}(R)\frac{u^2 - \overline{u^2}}{R}}_{\text{CFA}} + \underbrace{\left(\frac{\partial}{\partial z}K_v\frac{\partial v}{\partial z} + \frac{\tau_{b,y}}{\rho H}\right)}_{\text{friction}}, \tag{3}$$

with an overbar representing the depth average, and $\overline{v} = 0$ by definition. The lateral and vertical advection terms have been neglected. The term $\tau_{b,y} = K_v(\partial_v/\partial z)|_{\mathrm{bed}}$ is the lateral component of the bed shear stress, and surface stress is zero in the model. Variable H is water depth, and ρ is density. The first term on the left side is the unsteady term (time rate of change). The second term represents streamwise advection, i.e., the downstream adjustment of secondary circulation (e.g., Nidzieko et al. 2009). The first term on the right side is the baroclinic pressure gradient force (BCPG), and the second term is the centrifugal acceleration (CFA), and the third term is friction.

2) VORTICITY EQUATIONS

In addition to the momentum balance, we use the streamwise component of vorticity ω_x to quantify secondary circulation following Becherer et al. (2015). The vertical shear of lateral velocity usually dominates over the lateral shear of vertical velocity in determining ω_x, since $v \gg w$ and $\Delta y \gg \Delta z$. In a similar way, we can identify the lateral component of vorticity ω_y as the vertical shear of streamwise velocity. Therefore, we write

$$\omega_x = \frac{\partial w}{\partial y} - \frac{\partial v}{\partial z} \approx -\frac{\partial v}{\partial z}; \tag{4a}$$

$$\omega_y = \frac{\partial u}{\partial z} - \frac{\partial w}{\partial x} \approx \frac{\partial u}{\partial z}. \tag{4b}$$

Taking the vertical derivative of (1), substituting in (4), and rearranging

$$\frac{D\omega_x}{Dt} = -\beta g\frac{\partial s}{\partial y} + \frac{\partial v}{\partial x}\omega_y - \left(\frac{\partial v}{\partial y} + \frac{\partial w}{\partial z}\right)\omega_x + \mathrm{sgn}(R)\frac{2}{R}u\omega_y + \mathcal{R}_{\omega_x}; \tag{5a}$$

$$\frac{D\omega_y}{Dt} = \beta g\frac{\partial s}{\partial x} + \frac{\partial u}{\partial y}\omega_x - \left(\frac{\partial u}{\partial x} + \frac{\partial w}{\partial z}\right)\omega_y - \mathrm{sgn}(R)\frac{1}{R}u\omega_x + \mathcal{R}_{\omega_y}. \tag{5b}$$

The equation for ω_x (5a) is essentially a representation of the lateral momentum balance (3). While the momentum balance straightforwardly shows the terms responsible for lateral flows, the vorticity approach can provide a more consistent framework for understanding the generation and interaction of vorticity components (Becherer et al. 2015), and vorticity directly links to the vertical shear that affects mixing processes. Note that in (5), we have written out the baroclinicity, vorticity twisting, vorticity stretching (associated with divergence/convergence), and curvature terms, and we collect the remaining terms in $\mathcal{R}_{\omega_x}$ and $\mathcal{R}_{\omega_y}$, e.g., turbulent viscosity (friction).

3) WATER COLUMN STABILITY

We apply a gradient Richardson number analysis in a similar manner as Collignon and Stacey (2013) to investigate the effects of secondary circulation on stability and mixing. The gradient Richardson number Ri_g is defined as

$$\mathrm{Ri}_g = \frac{N^2}{S^2} = \frac{-\beta g \dfrac{\partial s}{\partial z}}{\left(\dfrac{\partial u}{\partial z}\right)^2 + \left(\dfrac{\partial v}{\partial z}\right)^2}, \tag{6}$$

where S is the total vertical shear, and N is the buoyancy frequency.

$$N = \left(-\frac{g}{\rho_0}\frac{\partial \rho}{\partial z}\right)^{1/2} = \left(-\beta g \frac{\partial s}{\partial z}\right)^{1/2}, \tag{7}$$

as temperature is uniform in the model and the density only depends on salinity. The Ri_g compares the stabilizing effect of stratification to the destabilizing effect of vertical shear (Miles 1961; Collignon and Stacey 2013). A critical value $\mathrm{Ri}_{g,\mathrm{cr}} \approx 0.25$ is used for determining the growth of instability in the water column (Miles 1961; Howard 1961). Shear can overcome stratification when $\mathrm{Ri}_g < \mathrm{Ri}_{g,\mathrm{cr}}$, which allows for the growth of turbulence and mixing; stratification damps instabilities when $\mathrm{Ri}_g > \mathrm{Ri}_{g,\mathrm{cr}}$ such that turbulence and mixing are inhibited.

The tendency equation for Ri_g is assessed to identify the influences of secondary circulation on water column stability and mixing by taking the derivative of (6):

$$\frac{D\mathrm{Ri}_g}{Dt} = \frac{1}{S^2}\left[-\beta g \frac{D}{Dt}\left(\frac{\partial s}{\partial z}\right) - 2\mathrm{Ri}_g \frac{\partial u}{\partial z}\frac{D}{Dt}\left(\frac{\partial u}{\partial z}\right) - 2\mathrm{Ri}_g \frac{\partial v}{\partial z}\frac{D}{Dt}\left(\frac{\partial v}{\partial z}\right)\right]. \tag{8}$$

The first term on the right side corresponds to the tendency of the vertical salinity gradient $\partial s/\partial z$. The other two terms correspond to the tendency of vertical shear, which depends on the vorticity dynamics in (5). The evolution of $\partial s/\partial z$ can be written as

$$\frac{D}{Dt}\left(\frac{\partial s}{\partial z}\right) = -\frac{\partial u}{\partial z}\frac{\partial s}{\partial x} - \frac{\partial v}{\partial z}\frac{\partial s}{\partial y} - \frac{\partial w}{\partial z}\frac{\partial s}{\partial z} + \mathcal{R}_{\mathcal{S}}, \tag{9}$$

which is found by taking the vertical derivative of salinity transport equation. The first two terms on the right side represent the straining of horizontal salinity gradients by the vertically sheared horizontal flow. The third term represents the stretching (compressing) of vertical salinity gradients associated with vertical divergence (convergence). Note that this stretching/compressing term is the normal straining of vertical salinity gradients, and we name it in this way to avoid confusion with the shear straining described by the first two terms. Vertical mixing is collected in the remainder term $\mathcal{R}_{\mathcal{S}}$.

Substituting (4), (5), and (9) into (8), we can therefore quantitatively characterize the competing effects of vertical shear and salinity gradients on Ri_g:

$$\begin{aligned}\frac{D\mathrm{Ri}_g}{Dt} = \frac{1}{S^2}\Bigg\{ & \underbrace{\beta g\left(-\omega_x\frac{\partial s}{\partial y} + \omega_y\frac{\partial s}{\partial x}\right)}_{\text{salinity strain.}} + \underbrace{2\mathrm{Ri}_g\beta g\left(\omega_x\frac{\partial s}{\partial y} - \omega_y\frac{\partial s}{\partial x}\right)}_{\text{shear, baroc.}} \\ & \underbrace{-2\mathrm{Ri}_g\omega_x\omega_y\left(\frac{\partial u}{\partial y} + \frac{\partial v}{\partial x}\right)}_{\text{shear, twist.}} + \underbrace{\beta g\frac{\partial w}{\partial z}\frac{\partial s}{\partial z}}_{\text{salinity stretch.}} \\ & \underbrace{+2\mathrm{Ri}_g\left[\left(\frac{\partial v}{\partial y} + \frac{\partial w}{\partial z}\right)\omega_x^2 + \left(\frac{\partial u}{\partial x} + \frac{\partial w}{\partial z}\right)\omega_y^2\right]}_{\text{shear, stretch.}} \\ & \underbrace{-2\mathrm{Ri}_g\omega_x\omega_y\,\mathrm{sgn}(R)\frac{u}{R}}_{\text{shear, curv.}} + \mathcal{R}_{\mathcal{R}_{\mathcal{I}}}\Bigg\}\end{aligned} \tag{10}$$

The first term on the right side represents the salinity straining processes that affect Ri_g by creating stratification. Horizontal salinity gradients cannot only be converted to stratification by straining, but also have a tendency to drive gravity currents and enhance the shear through baroclinicity, and this shear generation process is represented by the second term. The third term on the right side results from the interplay of vorticity components (the twisting of horizontal shear into vertical shear). The fourth term corresponds to the effects of stretching/compressing of vertical salinity gradients on Ri_g. The fifth term represents the influence of divergence/convergence on vertical shear. The sixth term represents contributions from channel curvature. The remainder term $\mathcal{R}_{\mathcal{R}_{\mathcal{I}}}$ involves the effects of $\mathcal{R}_{\omega_x}$, $\mathcal{R}_{\omega_y}$, and $\mathcal{R}_{\mathcal{S}}$ on Ri_g, e.g., turbulent mixing of salinity and the turbulent viscosity (mixing of momentum). The potential influences of these terms on Ri_g dynamics will be discussed later. Through the Ri_g tendency analysis, we can assess the water column stability by incorporating both the salinity straining and the stretching/compressing that affect stratification and the different sources of shear that cause turbulence.

Note that the first and second terms on the right side of (10) are similar expressions but have opposite signs because horizontal salinity gradients have competing influences on Ri_g. Straining of horizontal salinity gradients can create stratification that stabilizes the water column while vertical shear due to a gravity current can induce turbulence and reduce stability. The first two terms can thus be rewritten as $(1 - 2\mathrm{Ri}_g)$ times the horizontal salinity gradient and vertical shear. These two terms alone would lead to a net tendency to decrease Ri_g to 0.5 for $\mathrm{Ri}_g > 0.5$, which can explain the Ri_g dynamics for a freely propagating 2D gravity current with a uniform horizontal density gradient (Simpson and Linden 1989).

4) VERTICAL SALINITY VARIANCE BUDGET

To assess the overall influence of secondary circulation and tidal intrusion fronts on stratification we use the vertical salinity variance budget. The depth-integrated vertical salinity variance budget (Burchard and Rennau 2008; Li et al. 2018) is

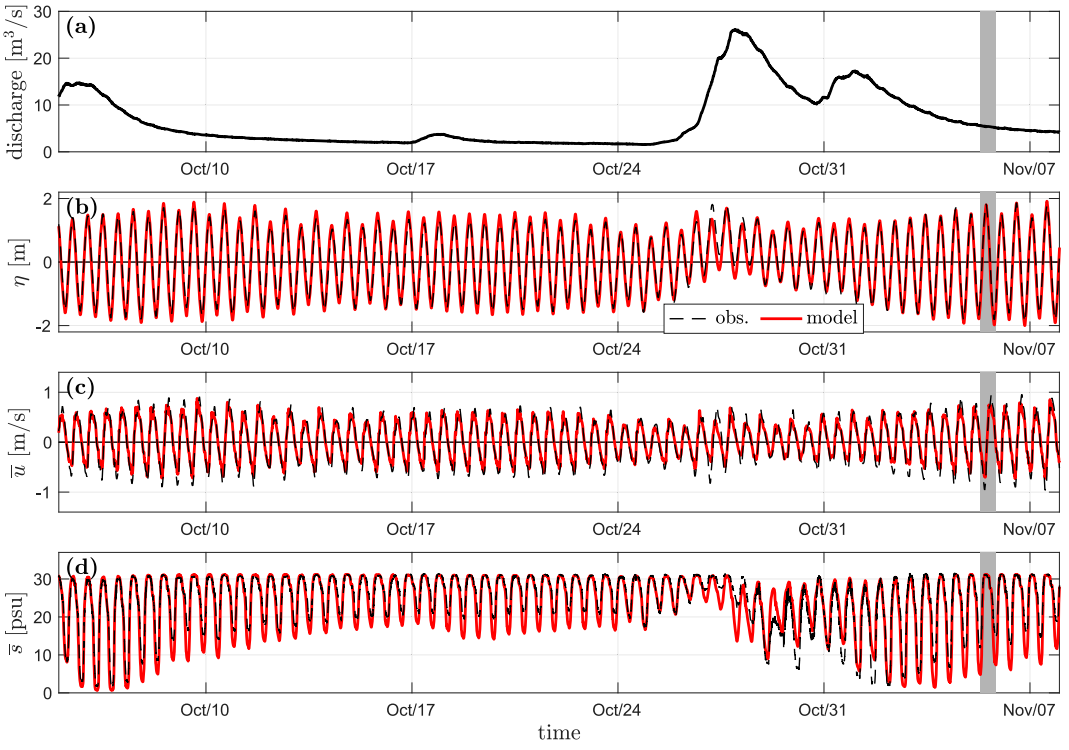

FIG. 2. (a) North River discharge in October and November 2021. (b)–(d) The modeled estuarine conditions compared with observations at the mooring site near the constriction (around 2 km into the estuary). Red lines represent model results, and dashed black lines represent observations. (b) Water level η. (c) Depth-averaged velocity $\overline{u}$. Negative u means landward velocity (flood direction). (d) Depth-averaged salinity $\overline{s}$. Gray bands show the tidal cycle selected for detailed analysis. Additional model–data comparisons are provided in the supplemental material.

$$\underbrace{\frac{\partial}{\partial t}\int (s_v')^2 dz}_{\text{unsteady}} = \underbrace{-\nabla_h \cdot \int \mathbf{u}(s_v')^2 dz}_{\text{advection}} \underbrace{- \int 2\mathbf{u}_v' s_v' . \nabla_h \overline{S} dz}_{\text{straining}}$$

$$\underbrace{- \int 2K_s \left(\frac{\partial s}{\partial z}\right)^2 dz}_{\text{turb.mixing}} \underbrace{- \int \mathcal{M}_{\text{num}} dz}_{\text{num. mixing}} . \qquad (11)$$

The term $\overline{s}$ is the depth-averaged salinity, and s_v' is the deviation from the depth average. The term $(s_v')^2$ is the vertical salinity variance that corresponds with stratification in the water column. The ∇_h is the horizontal gradient operator, $\mathbf{u} = (u, v)$ is the horizontal velocity vector, and $\mathbf{u}_v'$ represents the vertical deviations of horizontal velocity. Variable K_s is the eddy diffusivity for vertical salinity mixing. The left-side term represents the temporal change of the vertical salinity variance. The first term on the right side represents advection, and the second term represents straining [same as the shear straining process in (9) above, but here adapted for the vertical salinity variance]. The third term is turbulent mixing that irreversibly dissipates the vertical variance. The fourth term is the additional numerical mixing $\mathcal{M}_{\text{num}}$ that arises from discretization errors of the tracer advection scheme in the model. The numerical mixing $\mathcal{M}_{\text{num}}$ is calculated as the difference between the advected square of the tracer and the square of advected tracer (e.g., Burchard and Rennau 2008; Ralston et al. 2017; Kalra et al. 2019).

3. Results and analysis

a. Estuarine conditions

During the observation period of October and November 2021, the tidal range in the North River estuary was between 2 and 4 m, with a tidal velocity amplitude of 0.4–0.8 m s^{-1} (Fig. 2). The tides in this system are dominated by the semidiurnal M_2 tidal constituent, with stronger and weaker spring–neap tides each lunar month due to the semidiurnal S_2 and N_2 tidal constituents. During the study period, stronger spring tides occurred in early October and early November. A storm event in late October caused the subtidal water level to increase by 0.7 m due during the weak neap tide and increased the freshwater discharge from background levels of 0–5 m^3 s^{-1} to a peak of 30 m^3 s^{-1}.

The salinity and stratification varied at tidal time scales at the mooring locations. The tidal maximum stratification (bottom–surface salinity difference) was typically 5–10 psu, and was up to 20 psu during the high discharge event (not shown).

b. Drone imagery of surface fronts

In this section, we present drone imagery of surface fronts at two locations during spring flood tides in October and November 2021. These observational results are primarily explained at a descriptive level to demonstrate the

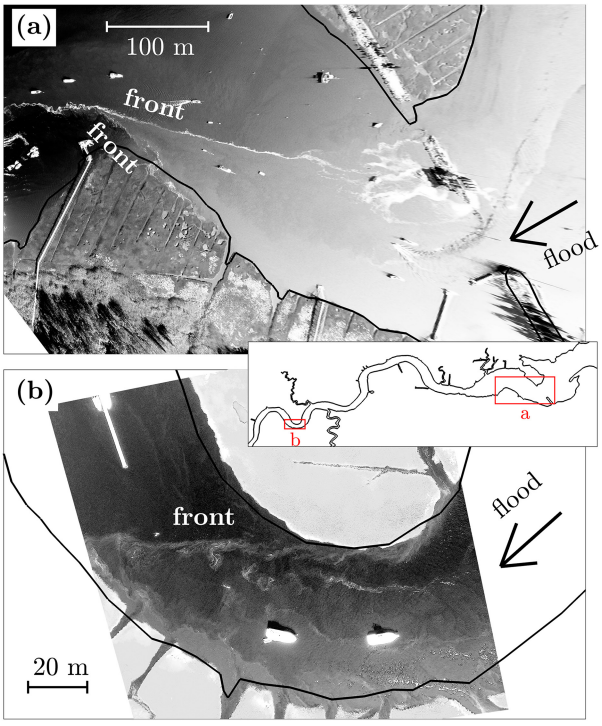

FIG. 3. Drone imagery during spring flood tides. (a) The constriction region at around 2 km into the estuary, at 1100 local time (LT) 7 Oct 2021. (b) A bend at around 5.5 km into the estuary (bend2 in Fig. 1), at 1200 LT 8 Oct 2021. Locations of the surveyed constriction and bend are shown by red rectangles on the map.

motivation for this study, and a more thorough analysis is conducted in the numerical model study in the following sections.

A V-shaped tidal intrusion front occurred downstream (landward) of the constriction at around 2 km into the estuary, as is shown in the drone imagery in Fig. 3a. The tidal flow through the constriction intruded into the ambient, lower-salinity water downstream of the constriction, leading to a V-shaped surface convergence zone with white foam accumulated on the surface. Higher velocities inside the V shape brought higher-salinity water landward through differential advection and created sharp salinity gradients across the V-shaped front.

Another example of surface fronts is shown in the drone imagery from a bend at around 5.5 km into the estuary (Fig. 3b, bend2 in Fig. 1). Flow separation occurred in the bend as a result of the curvature effect (Bo et al. 2021), with a low-velocity separation zone along the inner bank and higher streamwise velocities shifted toward the outer bend. Correspondingly, salinity was greater in the outer part of the bend as a result of differential advection. This lateral salinity gradient consequently formed an oblique surface front that could accumulate foam and debris, as seen in the drone image (Fig. 3b).

Detailed analysis of frontal dynamics will be presented in the following model investigation. Note that here the bend with drone imagery is located around 5.5 km into the estuary (bend2 in Fig. 1), whereas the bend selected for model analysis is at around 4 km (bend1 in Fig. 1). We have selected the bend at 4 km for model analysis because it exhibits stronger surface convergence and mixing than found in other bends, but the frontal processes are broadly similar in the different bends.

c. *Surface fronts and secondary circulation*

In this section, we analyze the tidal intrusion fronts and associated secondary circulation at a constriction and a bend in the numerical model. At both locations, flow separation occurs and creates lateral salinity gradients through differential advection. The lateral salinity gradients thus lead to secondary circulation in the cross section, which interacts with the salinity field and contributes to frontogenesis. The following analysis focuses on a stronger spring tide on 5 November as a representative of spring tide conditions when the surface fronts are most noticeable in the observations and in the model results.

1) THE CONSTRICTION

During flood tides, the tidal current is accelerated to over 1 m s^{-1} in the main opening as a result of the lateral constriction. Flow separation occurs on the landward side of the constriction, with strong lateral shear across the separation zones (Fig. 4). The high-velocity jet advects higher-salinity water to landward of the main opening, while lower-salinity water remains in the adjacent low-velocity zone. This differential advection creates sharp horizontal salinity gradients along with the strong lateral shear. Moreover, surface convergence occurs due to baroclinicity resulting from the horizontal salinity gradient, and two V-shaped surface fronts form downstream of the constriction (F1 and F2 in Fig. 4). The smaller V-shaped surface convergence front (F1) is attached to the narrow opening and the larger V-shaped front (F2) is over the shallow shoal farther downstream.

In a cross section through the V-shaped front at the constriction (XSC1 in Fig. 5), the jet flow brings higher salinity to the central channel, with a pair of lateral fronts on both sides due to flow separation. The salinity gradients across these lateral fronts lead to a pair of counterrotating secondary circulation cells. The circulation cell on the north side has southward velocity near the surface and northward velocity near the bed and the cell on the south side has an opposite sense of circulation. As a result, a surface convergence zone occurs near the center of the cross section, which corresponds to the V-shaped front F1 near the constriction in the map view (Fig. 4).

We examine the lateral momentum balance (3) in XSC1 to investigate the dynamics of the secondary circulation pattern (Fig. 6). The baroclinic pressure gradient (BCPG) associated with the lateral density variability is the dominant term in driving the pair of counterrotating circulation cells. The centrifugal acceleration (CFA) is less important since the curvature effect is relatively weak here. The frictional effect is weak in the channel center and increases on the shallower south side of the channel. Instead of friction, the BCPG is mainly

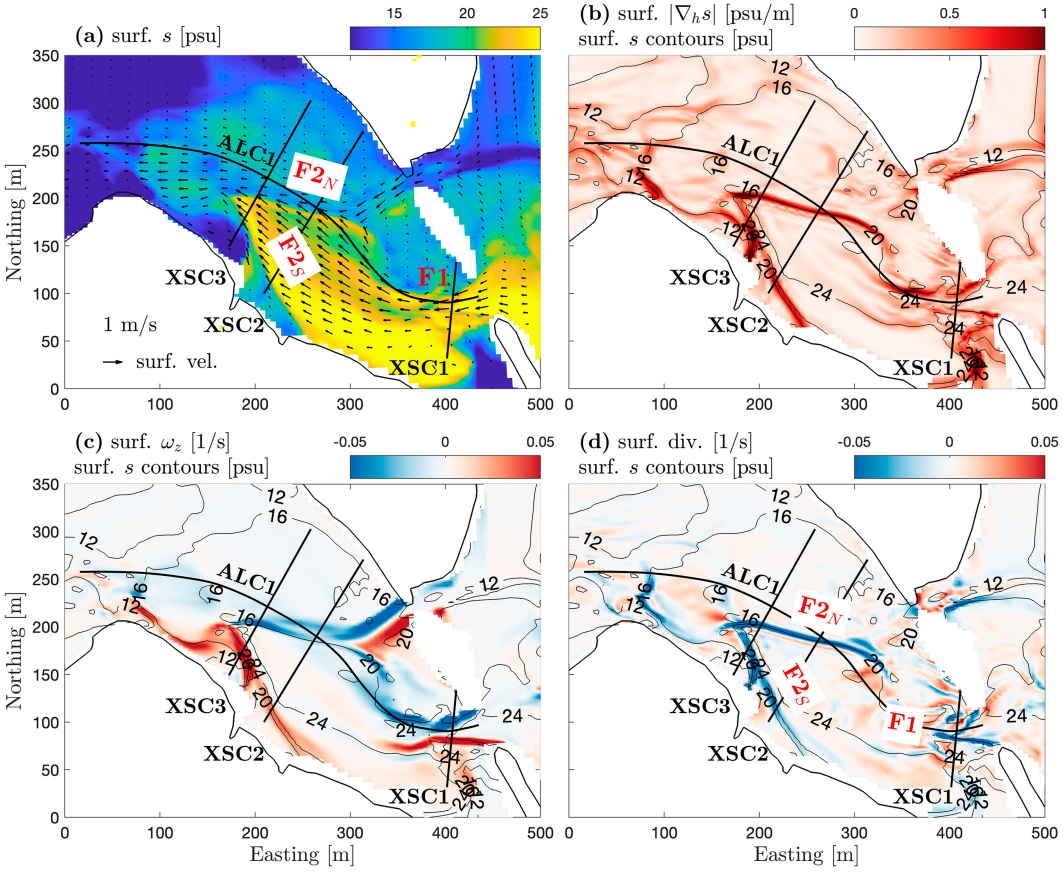

FIG. 4. Flow field in the constriction region at around 2 h into the flood tide. (a) Surface salinity. Arrows show surface velocity. (b) Horizontal gradients of surface salinity, with contours of surface salinity. (c) Vertical vorticity ω_z near the surface (curl of surface horizontal velocity). (d) Divergence of surface velocity, and blue colors represent surface convergence. Black lines show locations of the cross sections XSC1-3 and the along-channel section ALC1 taken for detailed analysis. The along-channel section is determined based on the streamline of the depth-averaged velocity, and the cross sections are orthogonal to the streamline. The red F1 in (a) and (d) marks the smaller V-shaped surface convergence front at the constriction, and F2$_N$ and F2$_S$ mark the north and south sides of the larger V-shaped surface convergence front landward of the constriction.

balanced by the advection term (downstream adjustment of secondary circulation) in this strongly advective system, consistent with Nidzieko et al. (2009) and Kranenburg et al. (2019). Given the dominance of BCPG in the lateral momentum balance, the secondary circulation is thus called BCPG-driven secondary circulation.

Farther landward, the jet flow expands as it encounters the shallower region downstream from the constriction (Figs. 1 and 4), and the two BCPG-driven secondary circulation cells and the corresponding surface convergence zones are separated farther apart (XSC2 in Fig. 5). Secondary circulation redistributes streamwise velocity in the cross section. Taking the lateral front in the northern part of XSC2 (front F2$_N$) as an example, the laterally sheared streamwise flow, with weaker velocity on the north side, is twisted into vertical shear by the counterclockwise secondary circulation. This downward and northward intrusion of high streamwise momentum leads to a reversal in vertical shear, with lower velocity in the upper water column. The BCPG-driven secondary circulation also laterally transports salinity near the front, with the near-bottom lateral flow advecting saltier water northward and the near-surface flow advecting fresher water southward. As a result, lateral salinity gradients initially created by differential advection are converted to vertical gradients by the secondary circulation, creating stratification through this lateral straining.

In addition to the creation of stratification, mixing that acts to destroy stratification also occurs at the north-side front in XSC2 (Fig. 5), and the detailed mechanism of mixing will be analyzed in the following sections. The front on the north side (F2$_N$) is in deeper water and is more representative of other tidal intrusion fronts in the system. The water column in the southern part of XSC2 is only 1–2 m deep (see front F2$_S$), and the greater influence of the bottom boundary leads to different mechanisms of frontal dynamics, which will be discussed later.

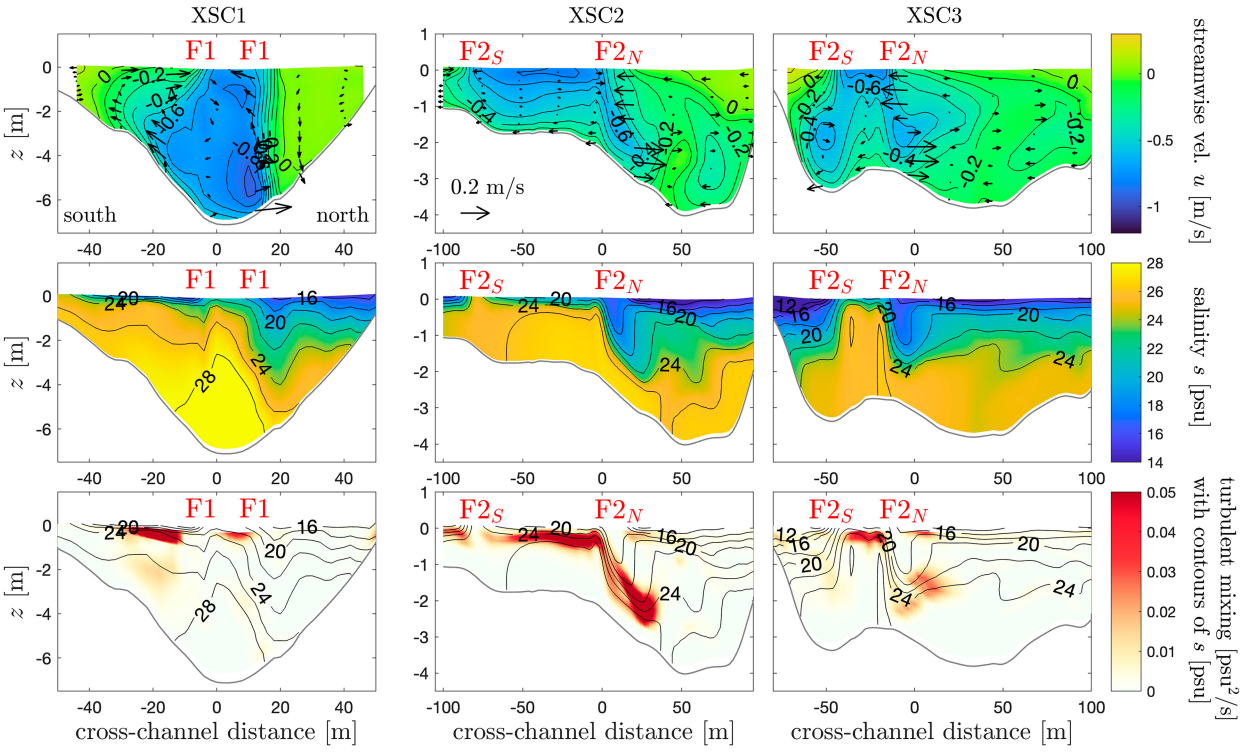

FIG. 5. Streamwise velocity u, salinity s, and mixing in cross sections XSC1, XSC2, and XSC3. Locations of cross sections are shown in the map views in Fig. 4. Negative u means landward velocity (flood direction). The southern bank is on the left side, with the flood current going into the page. Arrows show secondary circulation. Locations of the V-shaped surface convergence zones are marked by the red F1, $F2_N$, and $F2_S$.

The pair of lateral surface fronts ($F2_N$ and $F2_S$) converge near the center of the jet flow (e.g., comparing XSC2 and XSC3). The surface convergence zones are oblique to the streamwise current and form the second, larger V-shaped tidal intrusion front (Simpson and Nunes 1981; Largier 1992) (Fig. 4). The composite Froude number G for two-layer flow (e.g., Armi and Farmer 1986; Geyer and Ralston 2015) is examined to understand the oblique angle of the front.

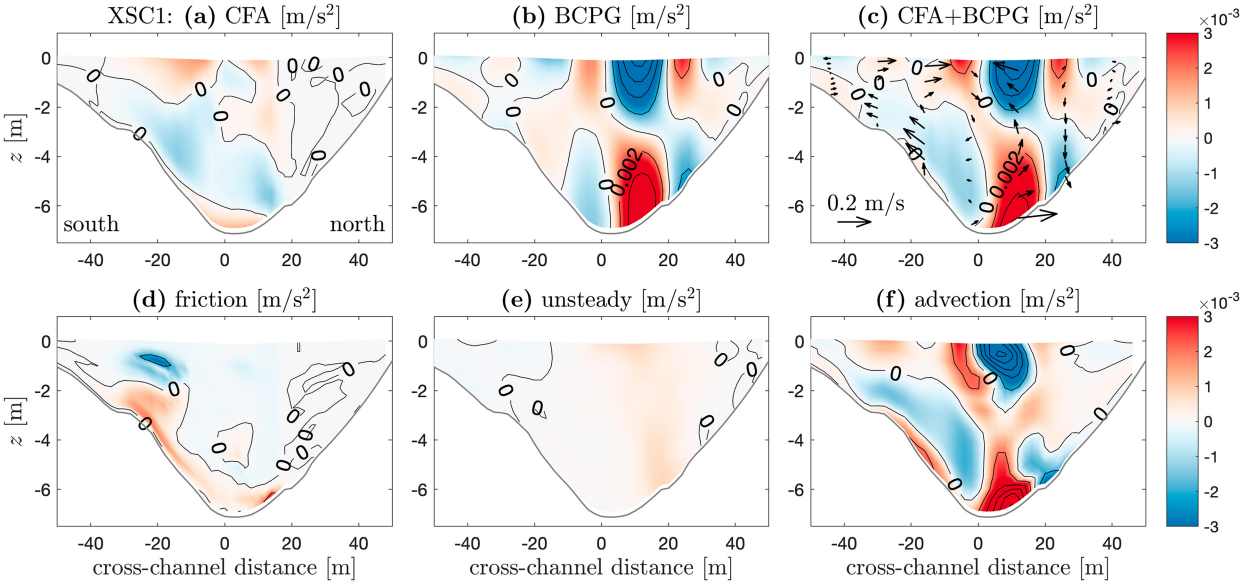

FIG. 6. Terms in the lateral momentum balance (3) in the cross section XSC1. Red colors mean northward (rightward) forcing, and blue colors mean southward (leftward) forcing.

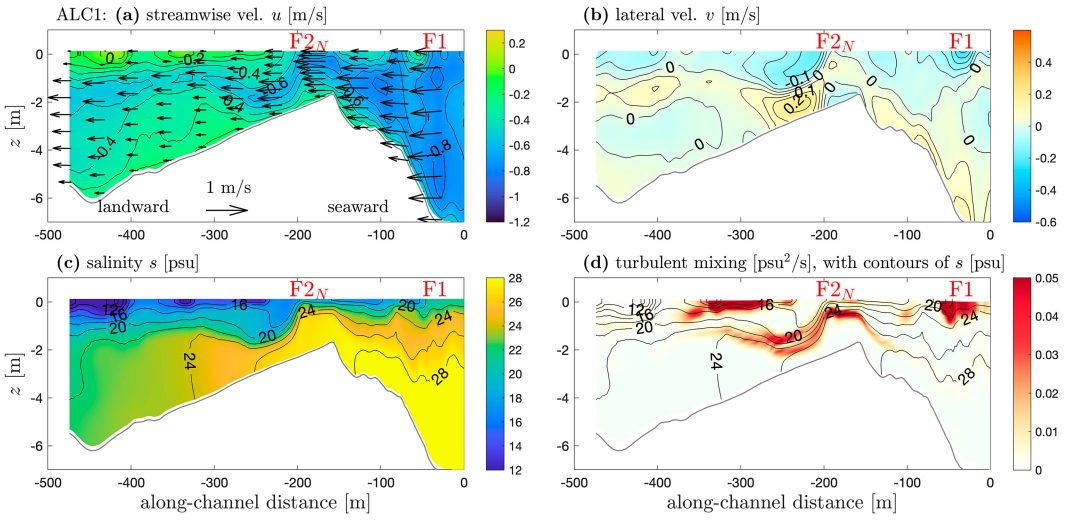

FIG. 7. The along-channel section ALC1 (location shown in Fig. 4). (a) Streamwise velocity u. (b) Lateral velocity v. Positive v is northward. (c) Salinity s. (d) Mixing, with contours of s. The red F1 and F2$_N$ show the locations of the V-shaped surface convergence zones. Negative distance means landward direction, and the constriction opening is at 0 m.

$$G^2 = \frac{u_1^2}{g' H_1} + \frac{u_2^2}{g' H_2}, \tag{12}$$

where u_1 and u_2 are the average velocities of the upper and lower layers, and H_1 and H_2 are the layer thickness. The term $g' = g(\Delta\rho/\overline{\rho})$ is the reduced gravity based on the density difference between the two layers. The composite Froude number based on the streamwise layer velocities is $G \approx 3$ at the front F2, indicating a supercritical condition. Nevertheless, the front is relatively stationary during several hours in the flood tide rather than moving landward with flood tidal currents. A stationary front can occur under a supercritical condition when it is oblique to the main flow direction such that the critical condition is satisfied in the direction normal to the front (Largier 1993; MacDonald and Geyer 2005; Geyer and Ralston 2015). In this case, the front F2 has an oblique angle $\phi \approx 20°$, so that the front-normal Froude number $G\sin\phi$ is close to 1, the critical condition.

Note that while tidal currents are usually slower over shallow regions due to topographic steering (e.g., Dietrich and Smith 1983), in this case, currents over the shoal inside of the V-shaped front F2 are faster than in the deeper region to the north. This demonstrates that the lateral shear across front F2 is associated with the jet flow from the narrow opening rather than due to topographic steering and the bottom frictional torque. As the jet flow transitions from the shallow shoal into deeper water, the composite Froude number decreases. A relatively stationary front is maintained at the channel–shoal transition where the composite Froude number decreases to the critical value of 1, with the oblique flow angle incorporated (front F2$_N$ in Fig. 7). The flooding streamwise flow of higher-salinity water subducts when encountering the surface front. The surface convergence at the front mainly results from the lateral circulation, but the streamwise flow that encounters the oblique front enhances the convergence at the surface as well.

While the V-shaped convergence zone on the surface is prominent both in the model and in the field, the flow and salinity fields associated with the tidal intrusion front are strongly 3D (see the cross sections in Fig. 5 and the along-channel section Fig. 7). The V-shaped surface convergence zone and 3D frontal structure are also generally consistent with observations from drone imagery (Fig. 3a) and shipboard measurements (see appendix A). Note that the snapshot in the model results corresponds to an earlier tidal stage (2 h into the flood, Fig. 4) than the drone imagery (3 h into the flood, Fig. 3). We provide a model snapshot from later in the tide that is similar to the V-shaped front observed in the drone imagery in appendix B (Fig. B1). The earlier snapshot is selected for detailed analysis because of the presence of stronger mixing at that time.

To summarize the frontal dynamics in the constriction region, flow separation occurs downstream of the narrow opening, with strong shear across the separation zones. The laterally sheared flow leads to the formation of sharp lateral salinity gradients through differential advection, resulting in lateral fronts. Secondary circulation occurs near the fronts driven by the baroclinic forcing. The secondary circulation both enhances the stratification and leads to intense mixing near the front, as will be analyzed in detail later. Secondary circulation also influences the horizontal velocity convergence, which can cause additional feedback on frontogenesis. The subsequent analysis of this study (sections 3d and 3e) focuses on the stratification and mixing associated with the front rather than the detailed interactions between frontogenesis and velocity convergence. In addition to this sharp constriction at the railroad embankment, similar tidal intrusion fronts also occur during the flood tide at other topographic features along the estuary where flow separation occurs, e.g.,

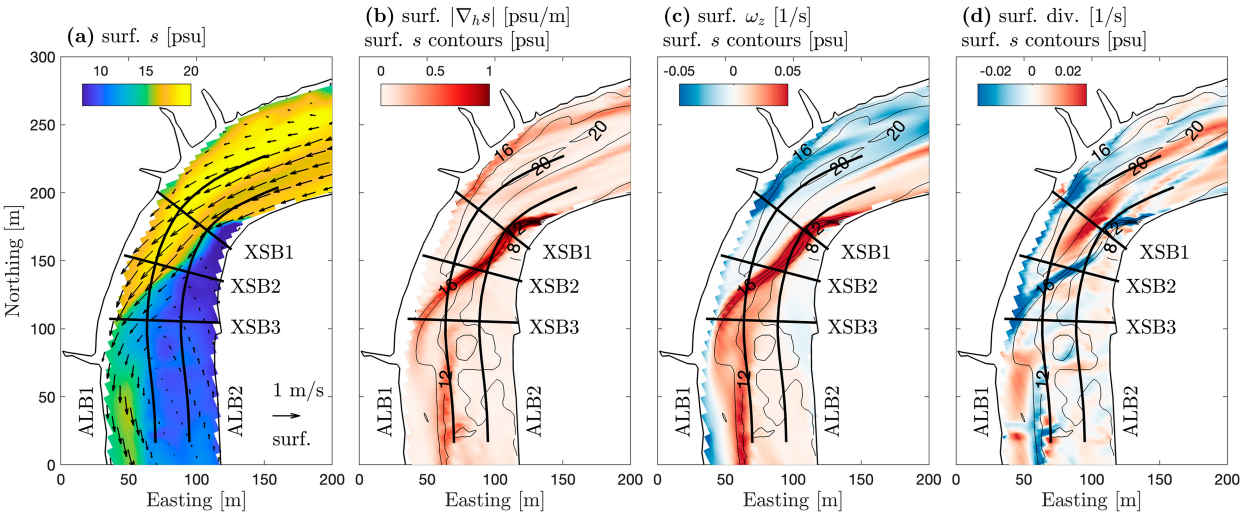

FIG. 8. Flow field in the bend region at around 3 h into the flood tide. (a) Surface salinity. Arrows show surface velocity. (b) Horizontal gradients of surface salinity, with contours of surface salinity. (c) Vertical vorticity ω_z near the surface (curl of surface horizontal velocity). (d) Divergence of surface velocity, and blue colors represent surface convergence. Black lines show locations of the cross sections and along-channel section taken for detailed analysis. The along-channel and cross-channel coordinates are established with reference to lines that are parallel and orthogonal to the channel centerline.

sand spits, island shoals, and in meanders [appendix B and section 3c(2)].

2) THE BEND

In the bend at around 4 km (bend1 in Fig. 1b), a surface front occurs as a result of flow separation and differential advection. The channel flow detaches from the inner bank at the bend apex, with a low-velocity separation zone formed near the inner bank in the lee of the bend (Fig. 8). The main flow is accelerated in the outer bend as it is restricted to a narrower part of the channel due to flow separation. As a result, salinity is higher near the outer bank and lower near the inner bank due to the differential advection of the along-estuary salinity gradient, leading to a sharp lateral front at the boundary of the separation zone.

In general, a single secondary circulation cell occurs in the cross section (Fig. 9) with outward velocity in the upper water column and inward velocity in the lower column. The lower salinity near the inner bank and higher salinity near the outer bank create BCPG forcing that is outward near the surface and inward near the bottom (e.g., at cross-channel distance of 0 m in XSB1 in Fig. 10), and this BCPG drives the counterclockwise secondary circulation. In addition, the CFA due to the curvature effect has comparable magnitude to the BCPG and a similar tendency to drive counterclockwise secondary circulation, with outward forcing near the surface and inward forcing near the bottom at 0 m cross-channel distance in XSB1.

The counterclockwise secondary circulation laterally transports lower salinity toward the outer bank near the surface (Fig. 9), so that the lateral surface front exhibits an oblique angle to the along-channel direction, spanning from the inner bank of the bend apex to the downstream outer bank (Fig. 8). In addition, the vertically sheared lateral velocity strains lateral salinity gradients into vertical gradients and thus increases stratification (Fig. 9). Likewise, secondary circulation also affects the distribution of streamwise velocity in the cross section. The slower-velocity separation zone expands outward near the surface, leading to slower velocity on top of faster velocity in the water column, i.e., the twisting of lateral shear into reversed vertical shear by the counterclockwise secondary circulation. Intense turbulent mixing occurs in the upper water column at the frontal boundary (Fig. 9), and the mechanism of mixing will be analyzed in the following sections along with that in the constriction region.

As the reversed vertical shear of streamwise velocity grows in the separation zone, i.e., slower velocity on top of faster velocity, the sense of CFA forcing is reversed in the lateral momentum budget (e.g., at −20 m cross-channel distance in XSB1 in Fig. 10, inward near the surface and outward in the lower column). This reversed CFA may reverse the sense of secondary circulation within the separation zone, leading to weak inward lateral velocity at the surface and outward velocity in the middle water column (e.g., from −40 to 0 m in XSB3 in Fig. 9). The reversal of CFA and secondary circulation in the separation zone is consistent with analysis of previous observations in this estuary (Kranenburg et al. 2019). The smaller, reversed (clockwise) secondary circulation cell at the inside of the bend has a weak tendency to decrease stratification in the separation zone, in contrast to the salinity straining and increased stratification associated with the counterclockwise secondary circulation on the outer side of the flow separation front. In addition, the reversed secondary circulation in the separation zone tends to convert vertical shear back to lateral shear, opposite to the shear twisting effect of the major counterclockwise secondary circulation.

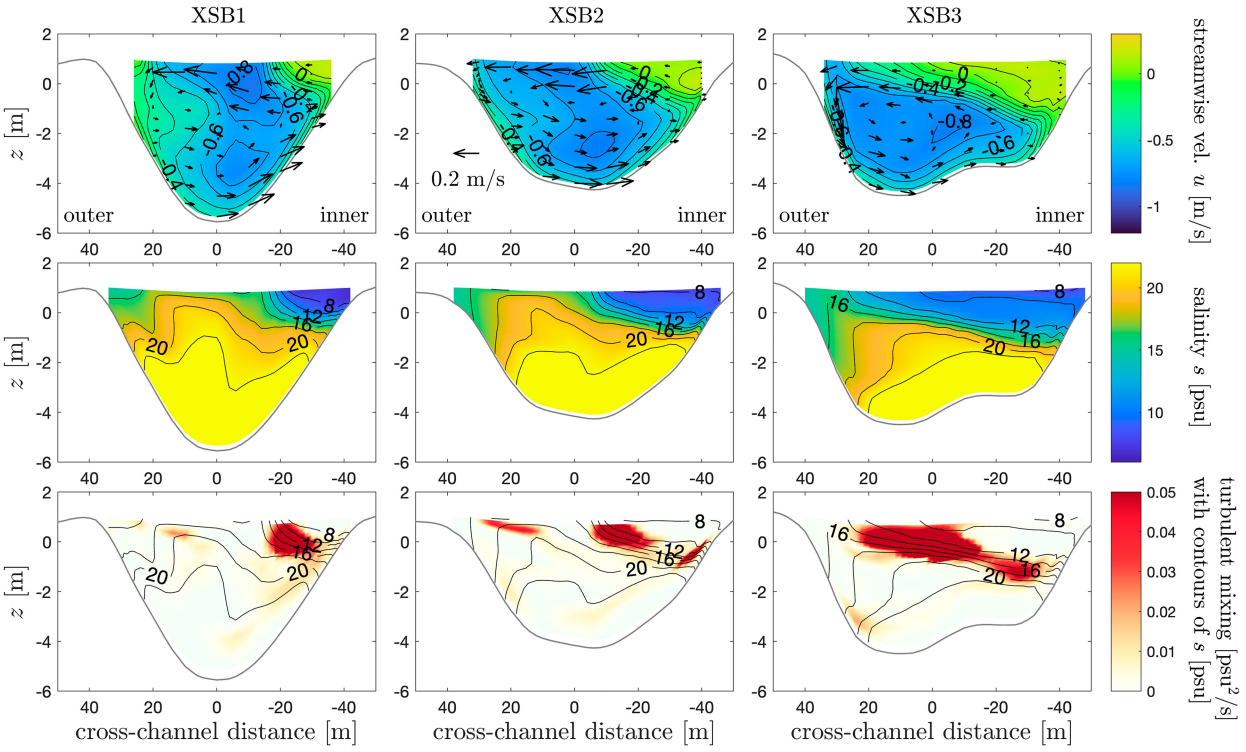

FIG. 9. Streamwise velocity u, salinity s, and mixing in cross sections XSB1, XSB2, and XSB3. Locations of cross sections are shown in Fig. 8. Arrows show secondary circulation. Negative u means landward velocity (flood direction). The inner bank is on the right side, with the flood current coming out of the page. Note that in these cross sections, $+y$ is leftward (outward) to ensure a right-hand coordinate system.

The reversal of CFA in the separation zone tends to create surface divergence near the front (e.g., at 0 to −20 m cross-channel distance in XSB1 in Fig. 10), counteracting the surface convergence due to the baroclinic effect at the front. The competing influences of the curvature effect (CFA) and the baroclinic effect are reflected in the discrepancy between surface horizontal salinity gradients and the surface convergence patterns downstream of the bend in the map view (Fig. 8). While generally surface convergences are correlated with sharp horizontal salinity gradients through baroclinicity, surface divergence occurs where the curvature effect locally exceeds the baroclinic effect, particularly near the bend apex.

Overall, the frontal dynamics, secondary circulation, and mixing in the bend region share similarities to the constriction region in that 1) a tidal intrusion front (surface convergence, Fig. 8) occurs due to flow separation; 2) the front is relatively stationary and has an oblique angle to the main channel flow direction; 3) secondary circulation strains the lateral salinity gradient and creates stratification (Fig. 9); 4) secondary circulation twists the laterally sheared streamwise flow at the lateral front and leads to reversed vertical shear in the upper water column; and 5) intense near-surface mixing occurs at the salinity front at the boundary of the flow separation zone (Figs. 9 and 11).

One major difference between the bend and the constriction is the mechanism of flow separation. In the constriction region, flow separation occurs on both sides of the jet flow from the narrow opening. In the bend, flow separation only occurs near the inner bank downstream of the bend apex due to the channel curvature effect (Leeder and Bridges 1975; Blanckaert 2015; Bo and Ralston 2020). As a result, a single surface front is created in the bend and instead of two fronts converging in a V shape as with the constriction. The fronts in both cases are oriented at an angle to the channel due to the Froude number constraint, so essentially the bend front resembles half of the V shape of the tidal intrusion at the constriction (Fig. 8).

Another major difference between the bend and the constriction lies in the driving force for secondary circulation in the lateral momentum balance (3) (XSB1 in Fig. 10). While the BCPG dominates over CFA in the constriction region, both terms are important for the lateral momentum balance in the bend. In the bend, both CFA and BCPG act to drive the counterclockwise secondary circulation near the lateral front, and CFA also create a smaller reversed (clockwise) secondary circulation cell in the separation zone. The additional CFA forcing due to channel curvature may create surface divergence near the front and thus act against the frontogenesis tendency of baroclinicity. The occurrence of reversed secondary circulation also adds complexity to the lateral salinity straining and shear twisting processes.

d. *Quantifying mixing and straining*

The vertical salinity variance budget (11) is calculated to quantitatively understand the influences of straining and mixing associated with surface fronts on stratification. In the constriction region, strong positive straining is found at the

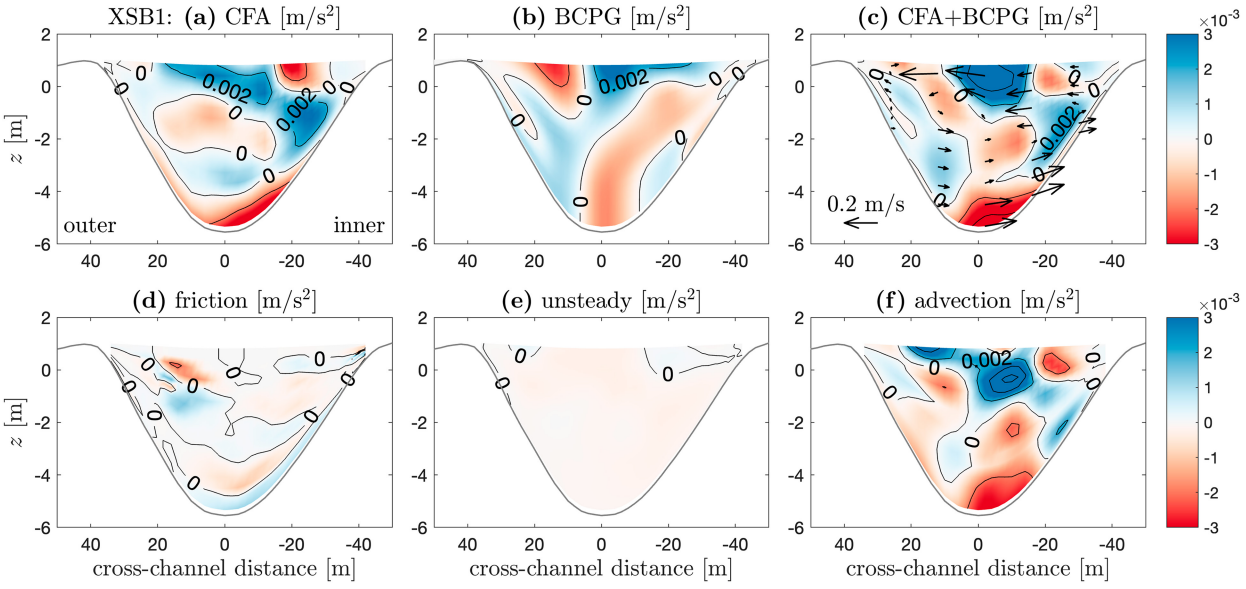

FIG. 10. Terms in the lateral momentum balance (3) in the cross section XSB1. The flood current is out of the page, and the inner bank is on the right side. Red colors mean inward (rightward) forcing, and blue colors mean outward (leftward) forcing. The advection term is placed on the left side of (3), so the momentum balance is achieved when the total forcing terms on the right side, primarily CFA and BCPG, equal the advection term. Note that here a positive value of forcing means leftward, because $+y$ is leftward (also see Fig. 9).

V-shaped tidal intrusion front, causing an increase in stratification (Fig. 12b). Locally, the straining term is dominantly due to the lateral component in (11), i.e., the interaction between vertical variations of lateral velocity and lateral salinity gradients. This positive straining in the variance budget converts lateral gradients to stratification through the BCPG-driven secondary circulation at the front (see the cross-sectional plots in Fig. 5). Note that some negative straining

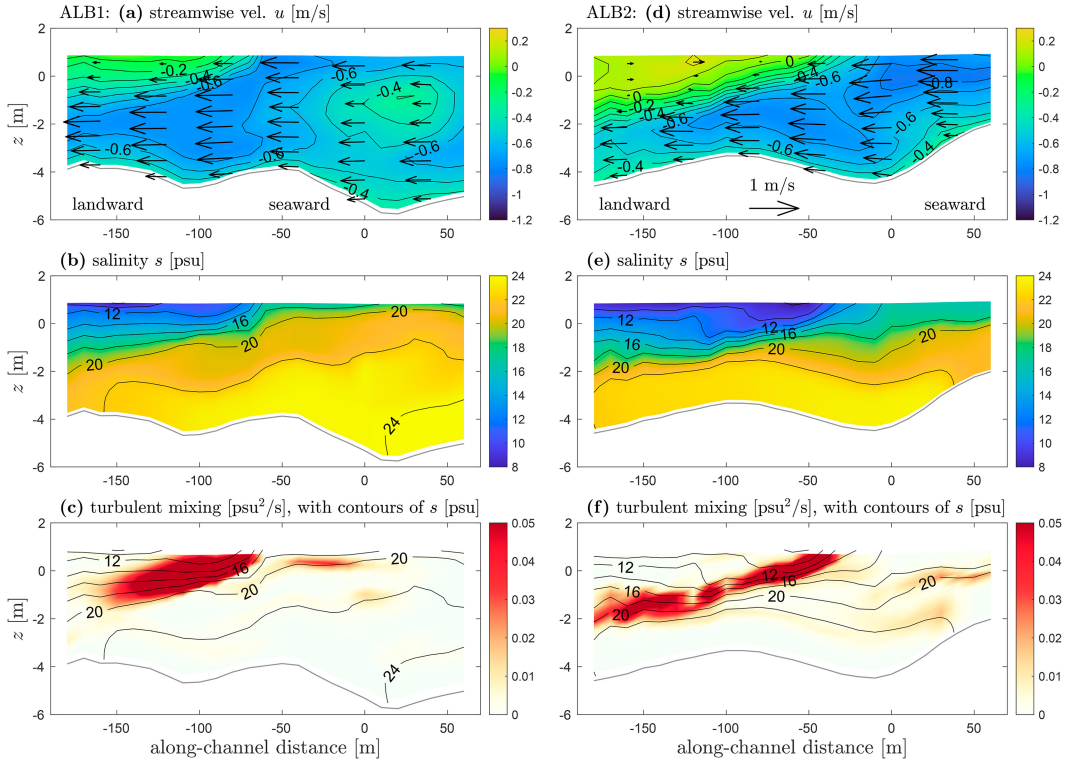

FIG. 11. Streamwise velocity u, salinity s, and mixing in along-channel sections ALB1 and ALB2. Locations of ALB1 and ALB2 are shown in Fig. 8. Negative distance means landward direction, and the bend apex is at 0 m.

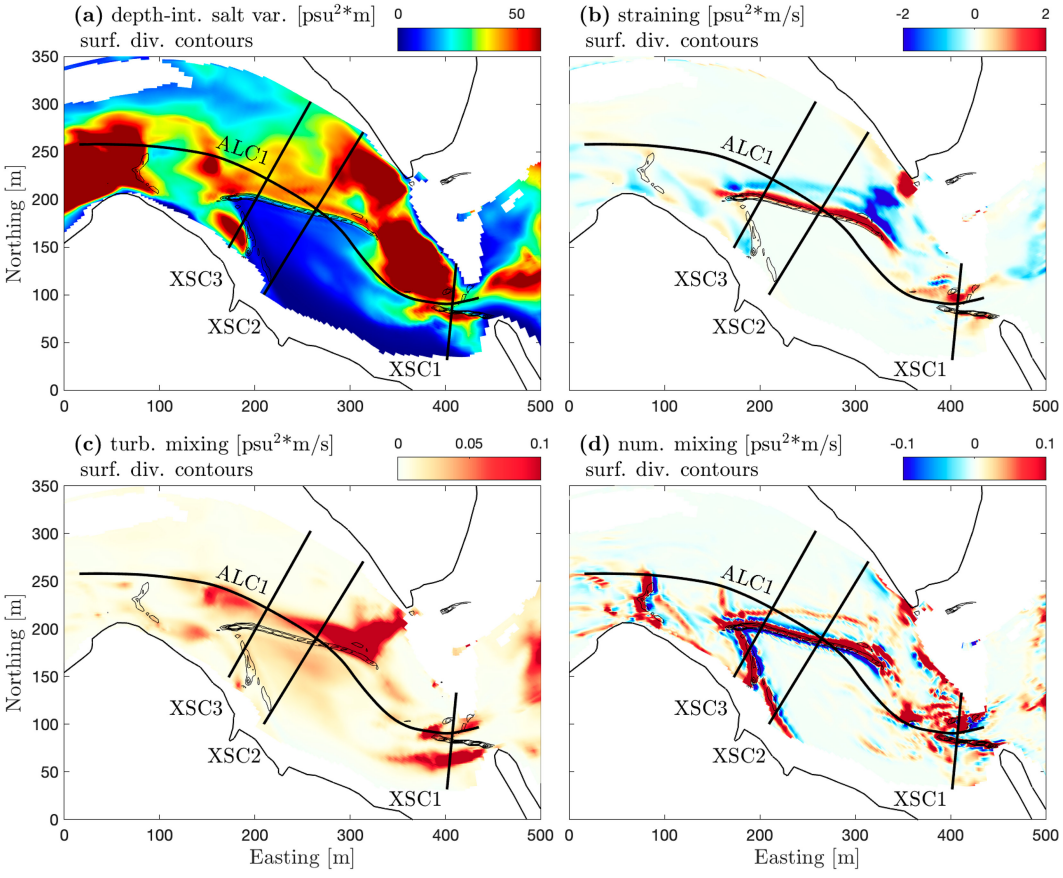

FIG. 12. Terms in the vertical salinity variance budget (11) in the constriction region. (a) Depth-integrated salinity variance, with contours of surface divergence. (b) Depth-integrated straining. (c) Depth-integrated turbulent mixing. (d) Depth-integrated numerical mixing. For mixing and numerical mixing, positive values (red colors) stand for destruction of stratification; for straining, positive values (red colors) stand for creation of stratification. Note the different color ranges of mixing and straining. The local magnitude of turbulent mixing can be much smaller than numerical mixing and straining, but their spatially integrated effects are comparable in the variance budget.

occurs north of the V-shaped front. This is because the downward velocity of secondary circulation locally suppresses the pycnocline and creates weak lateral salinity gradients north of the downwelling region, with higher salinity north of lower salinity (e.g., in the north part of XSC2 and XSC3 in Fig. 5). Negative straining occurs as the BCPG-driven lateral flows twist these weak lateral salinity gradients north of the front. Overall, positive straining at the front is much larger than negative straining north of the front, and the net effect of straining is to increase stratification.

While the positive straining at the tidal intrusion front is a source of stratification, the strong turbulent mixing near it tends to destroy salinity variance (Fig. 12c). Turbulent mixing is increased near the front due to the vertical shear and increased eddy diffusivity from the turbulence closure. While the strongest positive straining is collocated with the surface convergence front in the map view, the strongest turbulent mixing is adjacent to the convergence zone, outside of the V shape. This reflects the 3D structure of the front, as most of the turbulent mixing occurs away from the surface convergence where the frontal boundary extends into the water column (Figs. 5 and 7).

Additional dissipation of salinity variance occurs due to numerical mixing at the surface convergence zone where salinity gradients are sharpest (Fig. 12d). Numerical mixing can locally be either positive or negative, but the integration of numerical mixing is usually positive, i.e., an overall effect to decrease stratification. Numerical mixing results from the discretized tracer advection scheme in the model (Burchard and Rennau 2008). Generally, numerical mixing provides a proxy for the turbulent mixing that would happen in an actual frontal zone, where some salinity gradients occur within the grid scale and therefore cannot be resolved in the model (Ralston et al. 2017). Nevertheless, the consistency between model and observations (sections 3b and 3c and appendix A) indicates that numerical mixing provides a necessary contribution to the overall dissipation of salinity variance to yield realistic salinity fields.

Spatially integrating the variance budget over the constriction region, straining (mostly lateral straining) is the dominant

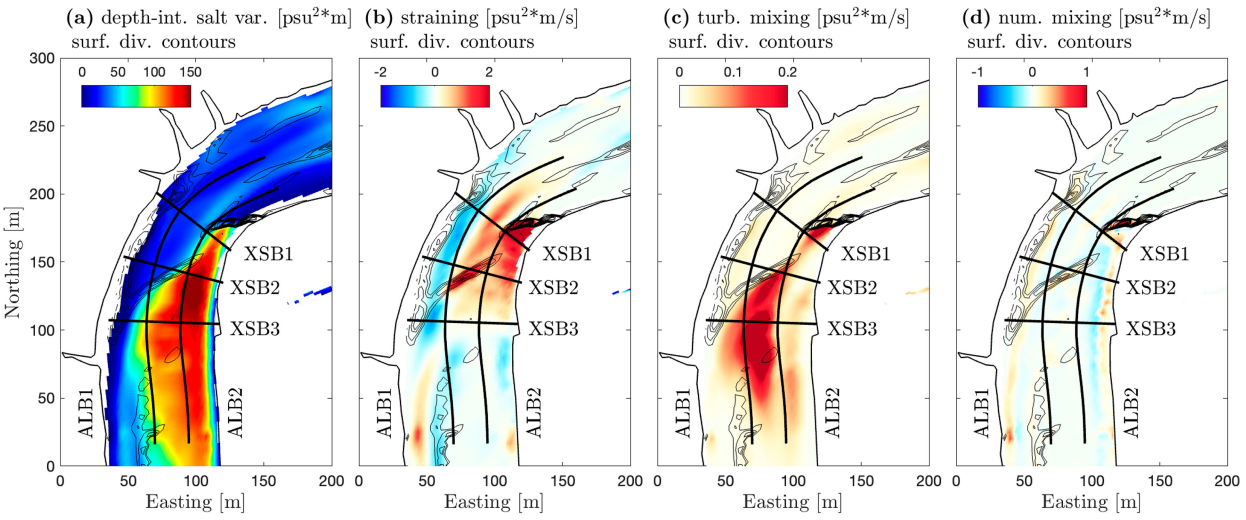

FIG. 13. Terms in the vertical salinity variance budget (11) in the bend region. (a) Depth-integrated salinity variance, with contours of surface divergence. (b) Depth-integrated straining. (c) Depth-integrated turbulent mixing. (d) Depth-integrated numerical mixing.

source of stratification during the flood tide. The created stratification is destroyed by the combination of turbulent mixing (60%) and numerical mixing (40%). Note that the total mixing generally balances with straining in the spatially and temporally integrated variance budget, but mixing and straining are not balanced locally and instantaneously, which thus leads to rapid creation or destruction of stratification near frontal zones.

In the bend region, straining and mixing have similar patterns as in the constriction. Intense positive straining occurs at the surface convergence front (Fig. 13b), which represents the creation of stratification by secondary circulation (see cross-sectional plots in Fig. 9). Regions with strong turbulent mixing are offset from the surface convergence zone in the map view (Fig. 13c), which corresponds to the enhanced mixing at the inclined, subsurface frontal zone (Figs. 9 and 11). Numerical mixing is weaker in the bend region compared to the constriction region. This is likely due to the less oblique front angle and the lower front-normal velocities in the bend, corresponding to weaker convergence and weaker horizontal salinity gradients. As a result, turbulent mixing accounts for 80% of the total mixing in the bend.

While the straining of salinity and creation of stratification associated with surface fronts has been reported in estuaries (e.g., Largier 1992; O'Donnell 1993; Giddings et al. 2012), the co-occurring mixing has received less attention. Our analysis suggests that strong turbulent mixing can happen near the surface convergence zone and tends to destroy the stratification created by straining. The horizontal salinity gradient across the front drives secondary circulation, which interacts with the salinity field to create stratification and with the streamwise velocity to create shear and turbulence. The occurrence of mixing near the front thus depends on the competition between these two processes, and the detailed mechanism of mixing will be examined in the following section.

e. *Stability and mixing at the front*

In this section, we investigate the dynamical processes that lead to turbulent mixing near the tidal intrusion front. The north-side front in XSC2 (at cross-channel distance of 0 to 50 m, the northern part of the V-shaped front $F2_N$) in the constriction region is selected as an example. Vertical shear is enhanced at the front (Fig. 14a), which provides a source of turbulence generation (Fig. 14d) and mixing (Fig. 5 XSC2). The enhanced vertical shear results from both the shear of lateral flow (longitudinal vorticity ω_x) and the shear of streamwise flow (lateral vorticity ω_y) (Figs. 14b,c).

The vorticity equations (5) are examined to understand the factors contributing to the vertical shear. The positive longitudinal vorticity ω_x at the front corresponds to the counterclockwise BCPG-driven secondary circulation downstream of the constriction. The ω_x is primarily forced by the lateral salinity gradient [see Fig. 14f and Eq. (5a)], consistent with the momentum balance analysis where the BCPG is dominant in driving secondary circulation [Eq. (3) and Fig. 6]. In the equation for the lateral vorticity ω_y [Eq. (5b)], the vorticity twisting (the third term) is most important for the creation of ω_y. Secondary circulation (ω_x) can twist the laterally sheared streamwise flow ($\partial u/\partial y$, i.e., part of the vertical vorticity, as Fig. 14e shows), and thus generate ω_y at the front. The along-channel salinity gradient in (5b) also has a tendency to increase ω_y, because the front is oblique to the jet flow from the constriction. However, this along-channel baroclinicity is weak because the orientation of the front is closer to the along-channel direction, and the lateral shear and lateral baroclinicity are more important.

Note that the lateral vorticity ω_y is positive at the front (Fig. 14c), and it corresponds to the reversed vertical shear of the streamwise current, i.e., slower flood current above faster flood current (also see Fig. 5). In contrast to the bottom boundary layer where the no-slip condition causes velocity to increase with distance above the bed and creates negative ω_y,

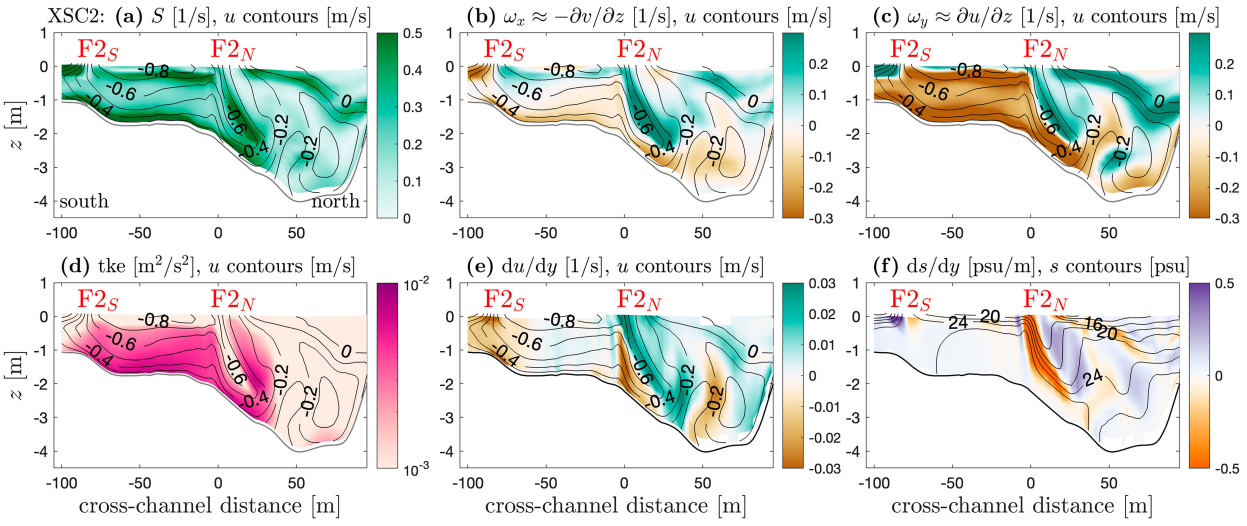

FIG. 14. (a) Total vertical shear S in the cross section XSC2, with contours of streamwise velocity. (b) ω_x (vertical shear of lateral velocity). (c) ω_y (vertical shear of streamwise velocity). (d) Turbulent kinetic energy tke. (e) Lateral shear of streamwise velocity. (f) Lateral salinity gradient, with contours of salinity s.

this reversed shear provides corroborating evidence that the pattern of shear and mixing is mainly associated with surface dynamics. Negative ω_y (normal shear) is found in the south part of XSC2 (Fig. 14c), because of the greater influence of the bottom boundary in this shallow region.

While strong shear created near the north-side front (F2$_N$) favors turbulence and mixing, stratification is also created there due to the straining of horizontal salinity gradients (section 3d), potentially stabilizing the water column and inhibiting turbulence. We examine the Ri$_g$ tendency equation (10) following a similar method to Collignon and Stacey (2013) to investigate the overall influence of frontal dynamics on water column stability.

The gradient Richardson number Ri$_g$ along a streamline through the frontal zone decreases from greater than 1 at the surface convergence zone to around the critical value Ri$_{g,\mathrm{cr}} \approx 0.25$ at the subducting frontal zone, thus allowing for turbulence and mixing (Figs. 15a–c). Note that the time derivative of Ri$_g$ in Eulerian coordinates is small compared to the advection terms, so Ri$_g$ is relatively steady in time at the stationary front. The decreasing trend of Ri$_g$ refers to the Lagrangian coordinates and is mostly associated with advection, i.e., the downstream decrease in Ri$_g$ along the streamline.

The straining of horizontal salinity gradients, primarily due to lateral straining, creates stratification and tends to increase Ri$_g$ (Fig. 15d). The horizontal salinity gradients also enhance the vertical shear through baroclinicity (primarily in the lateral direction), and thus tend to decrease Ri$_g$. The direct influences of horizontal salinity gradients on stratification and shear, i.e., the first two right-side terms in (10), have a net tendency to decrease Ri$_g$ to 0.5 rather than 0.25 (Simpson and Linden 1989). In addition, the vorticity twisting term contributes to decreasing Ri$_g$ [the third term in (10), primarily the twisting of lateral shear into vertical shear] as the laterally sheared jet flow from the constriction interacts with baroclinic secondary circulation. This tendency to decrease Ri$_g$ relates to the creation of reversed shear in the upper water column, as noted in the vorticity analysis above, and it contributes to around 1/3 of the total decreasing tendency of Ri$_g$ at the subducting front. The decreasing trend of Ri$_g$ thus tends to destabilize the water column, favoring the growth of turbulence and mixing near the front.

The overall influence of convergence/divergence on Ri$_g$ is small [salinity stretching and vortex stretching, the fourth and fifth terms in (10)], because their effects on vertical salinity gradients and vertical shear largely cancel each other in Ri$_g$. The influence of channel curvature on Ri$_g$ is generally negligible in the constriction region where curvature is mild (only considering the horizontal curvature effect here).

In addition to the mechanisms described above, other processes in the remainder term $\mathcal{R}_{\mathcal{R}_I}$ in (10), e.g., mixing, may also affect Ri$_g$. At the frontal zone, turbulent mixing of momentum (viscosity) tends to weaken the shear and increase Ri$_g$, while mixing of salinity tends to diffuse the salinity gradient and decrease Ri$_g$. Generally momentum mixing has a stronger influence on Ri$_g$ compared to salinity mixing because Ri$_g$ depends on the square of shear, and their integrated effect is to increase Ri$_g$ near the tidal intrusion front. The increasing tendency of Ri$_g$ due to mixing is minimal at the surface convergence zone where Ri$_g > 1$, and it is not sufficient to counteract the overall decreasing tendency of Ri$_g$ due to the integrated effects of baroclinicity, shear twisting, and salinity straining. However, the mixing effect is greater where Ri$_g$ is close to the critical value Ri$_{g,\mathrm{cr}}$, leading to an increasing trend of Ri$_g$ that counteracts other processes and can prevent Ri$_g$ from decreasing to less than Ri$_{g,\mathrm{cr}}$ (e.g., Trowbridge 1992; Geyer et al. 2017). Note that the overall impact of mixing is not explicitly expressed in (10) because quantifying the influence of numerical mixing on Ri$_g$ is challenging. We primarily refer to turbulent mixing in the discussion above, but in

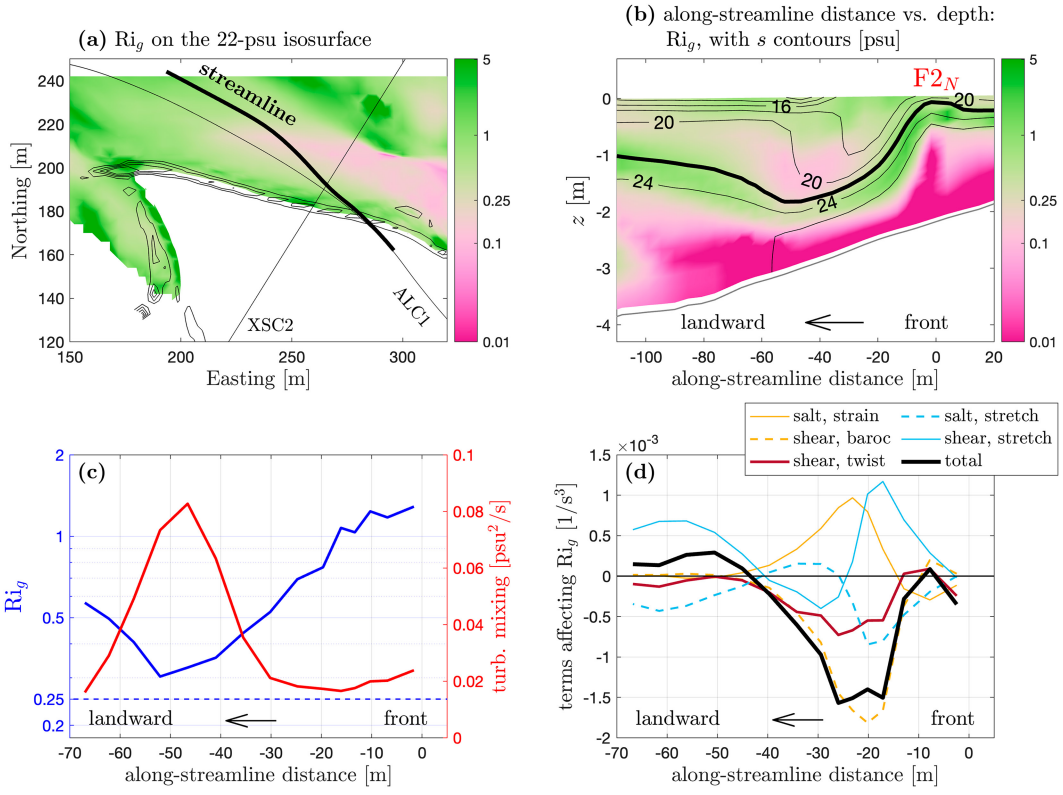

FIG. 15. Gradient Richardson number dynamics near the constriction. (a) Gradient Richardson number Ri_g on the 22-psu salinity isosurface. Black contours of surface convergence show the V-shaped surface front. The thick black line shows a 3D streamline with the starting point on the 22-psu isosurface. Note that the streamline subducts at the surface convergence front and generally follows the 22-psu isosurface. Thin black lines show the locations of the cross section XSC2 and the along-channel section ALC1 shown in Figs. 4, 5, and 7. (b) Ri_g on the along-streamline distance vs depth plot, with salinity contours. The 22-psu contour is thickened and it generally corresponds with the 3D streamline in (a). The surface convergence zone is at 0-m along-streamline distance. (c) Ri_g and turbulent mixing along the 3D streamline. Also refer to Fig. 5 XSC2 and Fig. 7. (d) Terms in the Ri_g tendency equation (10) along the 3D streamline, including the salinity straining and stretching/compressing terms that affect stratification, vertical shear generation due to baroclinicity, vertical shear generation due to twisting of horizontal shear, vertical shear generation (vortex stretching) associated with velocity divergence/convergence. See legend for details.

general numerical mixing is expected to act in a way similar to turbulent mixing.

In addition to the frontal zone, mixing also occurs over the shallow shoal in the southern part of XSC2 (Fig. 5, XSC2, at cross-channel distance from −50 to 0 m). The influence of frontal dynamics and secondary circulation on Ri_g, in particular salinity straining and shear twisting, is weaker over the shoal compared to near the front. Instead, the bottom boundary layer has a greater influence on Ri_g dynamics in this shallow region. As stratified water coming from the constriction encounters the shallow shoal, the strong bottom boundary shear and turbulence can decrease Ri_g and thus lead to mixing (i.e., mixing occurring inside the V shape in the map view Fig. 12c).

In the bend region, the processes that affect water column stability are mostly similar to the north-side front ($F2_N$) in the constriction region. The straining of salinity tends to increase Ri_g, and the baroclinic exchange and vorticity twisting tend to decrease Ri_g at the sharp lateral front where the major counterclockwise secondary circulation cell occurs (Fig. 9). Moreover, the curvature effect also contributes to enhancing the shear, decreasing Ri_g, and destabilizing the water column in the bend, which is consistent with the more prominent contribution of CFA in the lateral momentum balance [see Eq. (3) and Fig. 10]. Note that in the separation zone where the reversed (clockwise) secondary circulation cell occurs, the vorticity twisting term instead tends to twist vertical shear back into lateral shear and increase Ri_g locally (Fig. 9). In spite of the complexity of the smaller circulation cell within the separation zone, substantial mixing occurs near the frontal boundary where the counterclockwise secondary circulation occurs.

Overall, in both the constriction and bend regions, flow separation differentially advects salinity, interacts with secondary circulation, and leads to the generation of 3D frontal structures. Intense mixing occurs at both the constriction and bend fronts, because the combined effects of baroclinicity and twisting of shear by secondary circulation can enhance vertical shear and turbulence. Additionally, the curvature effect

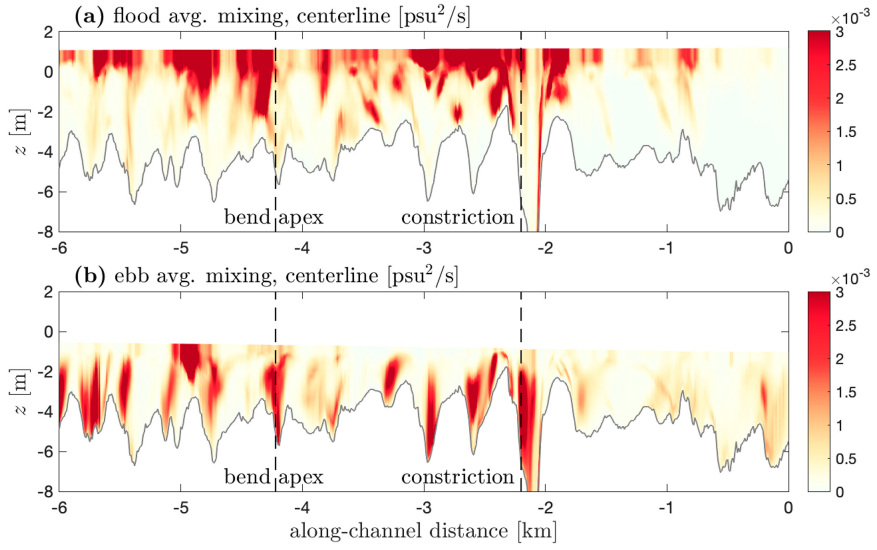

FIG. 16. Vertical distribution of mixing along the North River centerline, from the mouth to 6 km into the estuary. (a) Flood tide average. (b) Ebb tide average.

plays an important role in modulating convergence at the lateral salinity gradient through the bend.

f. The importance of near-surface mixing

The mixing associated with flood tide intrusion fronts occurs primarily in the upper water column, in contrast to bottom-generated turbulence and mixing that is usually dominant in shallow tidal estuaries without winds (e.g., Stacey et al. 1999; Geyer et al. 2000; Scully et al. 2011). To illustrate the tidal asymmetry in mixing, the time-averaged mixing along the North River centerline during the flood and ebb tide is compared in Fig. 16. During the ebb tide, the strongest mixing generally occurs in the lower water column in the bends, and that corresponds to bottom boundary layer mixing at bend-scale bottom salinity fronts created by the channel curvature effect as proposed by Bo and Ralston (2022). Note that an exception is found at around 5 km into the estuary where mixing is mostly near the surface during the ebb tide. A tributary creek merges into the main stem of the North River there (Garcia et al. 2022), and the plume of buoyant water from the creek leads to near-surface mixing locally during the ebb tide.

In contrast to the ebb tide when most of the mixing is associated with the bottom boundary layer, mixing during the flood tide occurs predominantly near the surface. We calculate the proportion of mixing that happens in and outside of the bottom boundary layer to assess the contribution of near-surface mixing. The bottom boundary layer height H_{bbl} is defined based on the vertical shear stress (Reynolds stress) distribution in a similar way to Stacey and Ralston (2005), with H_{bbl} being the distance above the bed where shear stress becomes smaller than 10% of the bottom shear stress. Integrating along the estuary from the mouth to the ~7 km region with large bottom roughness (excluding the marsh platform and tributary channels), around 80% of mixing during the flood tide happens above the bottom boundary layer. This contrasts with the mixing during the ebb tide, where around half of the mixing occurs within the bottom boundary layer and most of the rest is near the top of the bottom boundary layer.

In addition to the flood–ebb asymmetry in the vertical distribution of mixing in the water column, we also calculate the temporal distribution of mixing between flood and ebb tides. During the spring tide with moderate discharge examined here, around 60% of the mixing occurs during the flood and 40% of the mixing occurs during the ebb tide. With mixing mostly occurring in the upper water column during the flood tide, the near-surface mixing associated with tidal intrusion fronts is thus of comparable importance to bottom boundary layer mixing in this system.

4. Discussion

a. Key mechanisms

We investigated the tidal intrusion fronts that occur during flood tides near two types of topographic features, i.e., a constriction and a bend, as well as their influences on stratification and mixing. Downstream of the channel constriction, flow separation occurs on both sides of the jet flow from the narrow opening. The strong lateral shear zones between the jet and ambient flow create sharp lateral salinity gradients through differential advection. The resulting lateral baroclinic forcing leads to a pair of counterrotating secondary circulation cells with convergence near the surface. Driven by secondary circulation, the fresher ambient water on both sides of the saltier jet propagates toward the center near the surface (surface-converging lateral gravity currents). The competition between lateral surface currents and the along-channel jet flow leads to the oblique angle of surface fronts to the streamwise direction that have a nearly critical Froude number in the front-normal direction. As the saltier jet flow encounters

the frontal zone it subducts into the lower layer of landward flow. Therefore, a tidal intrusion front is generated downstream of the constriction, with a classical V-shaped convergence zone near the surface.

Stratification is created at the tidal intrusion front as a result of lateral straining by the BCPG-driven secondary circulation. While stratification is expected to inhibit turbulence and mixing, intense turbulent mixing is found near the front. Mixing occurs because both the vertical shear of secondary circulation and the reversed vertical shear of streamwise velocity contribute to decreasing Ri_g and destabilizing the water column. The reversed vertical shear of streamwise velocity, with the flood-tide current decreasing toward the water surface, results from the twisting of laterally sheared jet flow by the secondary circulation.

Analysis in the constriction region reveals that tidal intrusion fronts are hot spots of mixing, and similarly, channel bends can also lead to surface convergence fronts with intensified mixing. In the bend, flow separation occurs near the inner bank behind the bend apex as a result of the channel curvature effect. Similar to the constriction region, lateral salinity gradients are enhanced at the boundary of the separation zone as a result of differential advection and lead to secondary circulation through BCPG forcing. A tidal intrusion front occurs with the surface convergence zone being oblique to the main flow, spanning from the bend apex on the inner bank to the downstream outer bank. Enhanced mixing occurs at the tidal intrusion front in the upper water column, akin to the constriction region. In contrast to the V-shaped front downstream of the constriction, the tidal intrusion front in the bend resembles half of a V shape and can be regarded as a one-sided tidal intrusion front, since flow separation only occurs on the inner bank. Moreover, while the lateral BCPG dominates in the constriction region, the additional CFA due to the channel curvature effect has a comparable magnitude to BCPG in the bend. The combined influences of curvature and baroclinicity result in more complex secondary circulation, frontogenesis, vertical shear generation, and mixing.

Based on a salinity variance budget analysis, the mixing associated with tidal intrusion fronts is capable of destroying the stratification created by lateral straining. Furthermore, this mixing occurs predominantly near the surface during the flood tide, in contrast to the ebb tide when mixing mostly occurs in the lower water column. The flood tide near-surface mixing is found to be comparable to the bottom boundary layer mixing during the ebb tide in the North River estuary.

b. *Instability and mixing*

White and Helfrich (2013) conducted an idealized numerical study of a horizontal shear layer with a horizontal density gradient, and described two end-member regimes where instabilities can grow, i.e., a pure well-mixed horizontal shear layer and a pure gravity current without horizontal shear. Our analysis provides a realistic intermediate case between the two end-member regimes, where the interaction between lateral shear and lateral gravity current can generate a third component of vorticity, i.e., the reversed vertical shear of streamwise velocity near the surface, and this reversed shear is also important for destabilizing the water column and leading to turbulent mixing. The vorticity twisting and near-surface turbulence and mixing is also consistent with observations in Collignon and Stacey (2013) and Huguenard et al. (2015).

By contrast, Giddings et al. (2012) reported inhibition of turbulence near a lateral front in late flood tide. That could be a case where the additional reversed shear resulting from vorticity twisting was less influential because the streamwise tidal current was weak during the late flood stage. In those observations, the vertical shear of lateral gravity current alone was insufficient to overcome the stabilizing effect of stratification from straining.

Simpson and Linden (1989) found that for 2D gravity currents with a uniform horizontal density gradient, baroclinicity can only asymptotically decrease Ri_g to 0.5. To further decrease Ri_g and lead to the growth of instability, either nonuniformity in the horizontal density gradient (Simpson and Linden 1989) or velocity convergence due to topographic forcing (Geyer and Ralston 2015; Geyer et al. 2017) is needed [corresponding to the fourth and fifth terms in Eq. (10)]. As a comparison to the classical 2D scenario, the present study highlights the importance of 3D processes for decreasing Ri_g and leading to frontal instability and mixing, in particular the interaction between cross-front gravity currents (baroclinic secondary circulation) and alongfront background currents that was not represented in Simpson and Linden (1989).

This research suggests that the influence of flow curvature on water column instability and mixing is small in the constriction region. However, the channel curvature effect can be an important contributor to secondary circulation, enhanced vertical shear, and turbulence in channel bends, and thus provides an additional source of mixing in sinuous estuaries.

c. *Broader implications*

The analysis presented here focused on a spring tide with moderate discharge conditions and found that around 60% of the mixing occurs during the flood tide, primarily associated with surface fronts. In model results, the intensified mixing at surface fronts during flood tides consistently occurs across spring–neap cycles and under varying river forcing conditions. The fraction of the total mixing during flood tides varies between 30% and 60% during the simulation period, with the minimum flood-to-ebb ratio during neap tides with high river discharge in late October 2021. During that period, flood tide mixing still mostly happens near the surface and is associated with tidal intrusion fronts. Tidal currents (and thus the lateral shear) are weaker during neap tides, which leads to weaker differential advection and smaller lateral salinity gradients to drive secondary circulation and surface convergence. As corroborating evidence, the surface convergence features are generally less noticeable in both the model and observations during neap tides than spring tides. In addition, stronger stratification appears during that period due to the weaker tidal currents and higher river flow, and stratification can suppress secondary circulation (Chant and Wilson 1997) and thus

hinder the development of fronts and mixing. By contrast, intense mixing still occurs during the ebb stage when the pycnocline meets regions with strong bottom boundary turbulence, even with the stronger stratification. While the flood tide accounts for a smaller portion of the mixing during neap tides and high discharge, surface fronts remain an important factor in the total mixing and stratification in the estuary.

Similar near-surface mixing is also expected to occur in other estuaries where tidal intrusion fronts have been observed (e.g., Simpson and Nunes 1981; Largier 1992; Marmorino and Trump 1996). In particular, strong tidal currents and topographic features that can enhance the lateral shear are important for differential advection, frontogenesis, and mixing. Additionally, moderate stratification could favor the formation of fronts, as strong stratification may inhibit secondary circulation and thus the occurrence of convergence. With weak stratification, secondary circulation is still likely to occur, but it might lead to axial convergence fronts instead of classical tidal intrusion fronts (Nunes and Simpson 1985; Simpson and Turrell 1986).

Nunes and Simpson (1985) studied axial convergence fronts, and used an analytical solution to predict the strength of the associated secondary flow with the magnitude of lateral salinity gradient. We examined their analytical prediction with the tidal intrusion fronts and secondary circulation in our model. At the constriction, the analytical solution is generally effective in predicting the strength of secondary circulation based on the lateral salinity gradient due to differential advection. While the Nunes and Simpson (1985) solution assumed that the lateral pressure gradient forcing is balanced by friction, the frictional effect is relatively weak our results (Fig. 6), and the advection term replaces friction in balancing the pressure gradient forcing (Nidzieko et al. 2009; Kranenburg et al. 2019). In the bend region, the secondary circulation from the analytical prediction by Nunes and Simpson (1985) is correlated with the model results but has a much smaller magnitude. This discrepancy is likely due to the influence of the centrifugal forcing of flow curvature on the secondary circulation in addition to baroclinic forcing from differential advection.

Nevertheless, the correlation between the Nunes and Simpson (1985) solution and our model results indicates the intrinsic similarities between axial convergence fronts and tidal intrusion fronts, in terms of the lateral shear, differential advection, BCPG-driven secondary circulation, and surface convergence. We further speculate that the axial convergence front corresponds to an instance of the tidal intrusion front with weak stratification, even though they are named differently. The lateral gravity current propagation speed is small compared to the streamwise velocity when horizontal and vertical salinity gradients are weak, and the surface front thus resembles a single convergence line following the channel orientation, instead of exhibiting a conspicuous oblique angle to the upstream flow.

In addition, plume fronts were suggested to be dynamically related to tidal intrusion fronts as both have buoyancy-driven flow structures (O'Donnell 1993). Tidal intrusion fronts typically occur as saltier water is forced into estuaries by the strong flood tide current. The flood current may therefore oppose the motion of buoyant ambient water inside estuaries (moving at internal disturbance propagation speed), leading to a strong surface convergence zone with an oblique angle to the flood current. By comparison, in a river plume where fresher water discharges into saltier water, the internal disturbance propagation direction usually conforms to the direction of the inertial momentum of plume water. Therefore, the shape of a plume may be more dispersed on the surface compared to the V shape found in tidal intrusion fronts (Armi and Farmer 1986; Largier 1992). Nevertheless, the existence of ambient coastal current can introduce additional momentum that is against the plume, which may thus sharpen the shape of plume and lead to intense surface convergence and mixing (O'Donnell 1997; MacDonald and Geyer 2005).

5. Conclusions

We studied tidal intrusion fronts during flood tides in an estuary with complex topography, with a particular focus on two topographic features, i.e., channel constrictions and bends. Flow separation and differential advection are important for creating lateral salinity gradients at both locations, which drives secondary circulation through baroclinicity and generates surface convergence fronts, or tidal intrusion fronts. Secondary circulation creates stratification at fronts through lateral straining, and also enhances vertical shear through baroclinic exchange and twisting of the streamwise shear to lead to intense mixing near fronts. The constriction and bend regions have different frontal shapes as a result of differences in flow separation due to channel geometry. Moreover, channel curvature in bends also affects secondary circulation, frontogenesis, vertical shear, and mixing, along with baroclinicity. Overall, the near-surface mixing that is primarily associated with tidal intrusion fronts is similar in magnitude to bottom boundary layer mixing in this estuary.

Acknowledgments. The research leading to these results was funded by NSF Awards OCE-2123002 and OCE-1634481. The authors thank Peter Traykovski for providing the bathymetric data and Jay Sisson, Sean Whelan, Salme Cook, and Noa Randall for fieldwork assistance.

Data availability statement. Model data supporting this study are available online at https://doi.org/10.5281/zenodo.8126968; observational data are available online at https://doi.org/10.5281/zenodo.10059736.

APPENDIX A

Shipboard Surveys at the Constriction and Bend

During the observational period, shipboard surveys were conducted at multiple cross sections and along-channel sections near the constriction and in several bends in the North River estuary. Continuous salinity and temperature data were collected with a towed CTD array that had three or four CTD sensors in the vertical, and velocity profile data were collected with a shipboard acoustic Doppler current profiler.

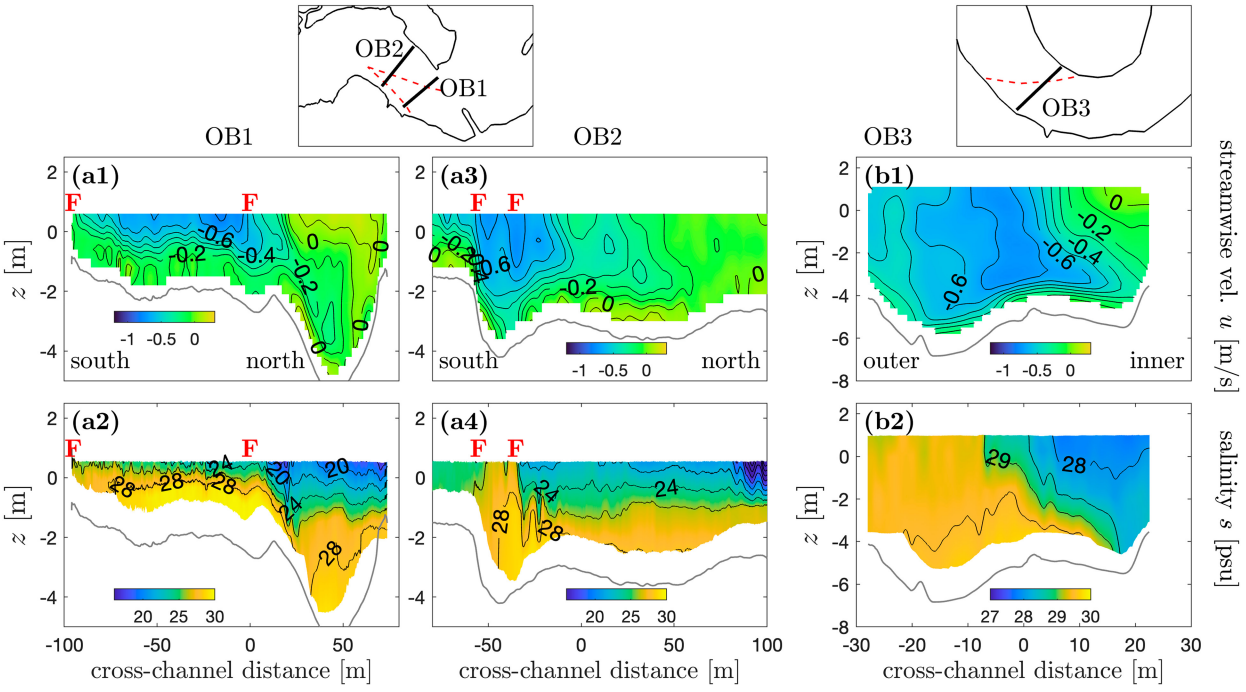

FIG. A1. Shipboard measurements of streamwise velocity and salinity during spring flood tides. (a1)–(a4) Two cross sections landward of the constriction at around 2 km into the estuary (at 1000 LT 7 Oct 2021). Negative velocity is landward (flood direction). The red "F" labels mark the V-shaped surface convergence front. (b1),(b2) A cross section in the bend at around 5.5 km into the estuary (at 1100 LT 5 Nov 2021). Locations of cross sections are shown on the small maps, with red lines delineating the surface fronts. Note that the shipboard measurements and drone surveys in Fig. 3 are conducted at different times but with similar tidal conditions and stages.

The sensor depths of the towed array were actively adjusted depending on the local bathymetry to maximize the vertical coverage, with a typical vertical spacing of 0.5–2 m between sensors. The towed array sampling was needed to resolve sharp density gradients at fronts better than possible with discrete CTD profiles.

Measurements in several representative cross sections are presented that correspond with regions and tidal stages with the occurrence of surface convergence fronts (Fig. A1). Landward of the constriction, faster velocity occurs on the southern part of the cross sections during the flood tide, which corresponds with the strong jet flow from the narrow opening (OB1 and OB2 in Fig. A1). The faster velocity brings higher-salinity water landward by differential advection and creates lateral salinity gradients across the lateral shear zones. The lateral salinity gradients can thus create secondary circulation and lead to the V-shaped surface convergence front (see the drone imagery in Fig. 3a), and the detailed mechanisms are explained in the numerical analysis (section 3c). Note that the V shape can also be inferred by comparing the width of the high-velocity and high-salinity region in OB1 and OB2. The velocity and salinity fields in the model (Fig. 5) are generally consistent with these observational results.

In the bend at around 5.5 km into the estuary, flow separation occurs during the flood tide at the bend apex and creates the low-velocity zone near the inner bank (OB3 in Fig. A1). The laterally sheared flow differentially advects salinity and thus leads to low salinity in the inner bank. The lateral salinity gradient contributes to the development of secondary circulation that can further interact with the main flow and generate the oblique surface convergence front (see the drone imagery in Fig. 3b; mechanisms examined in the model analysis in section 3c).

APPENDIX B

Modeled Surface Fronts at Multiple Locations

The snapshot shown in Fig. B1 is around 1 h later than that in Fig. 4. The V-shaped front shifts slightly landward by ~50–100 m and has a less oblique angle with respect to the main flow in this later snapshot. These shifts are primarily due to the weaker stratification later in the flood tide, which leads to an increased composite Froude number G. As a result, a more acute angle is required to satisfy the critical condition $G\sin\phi \approx 1$ at the front. The later snapshot is closer to the tidal stage when the drone imagery was captured, and the V-shaped front is more similar to the one shown in the drone imagery. Refer to the supplemental material for a movie of the model results in this region through a flood tide.

In addition to the constriction and bend regions discussed in the main text, surface convergence fronts also occur in other areas in the North River estuary. In a region between

the estuary mouth and the constriction, multiple V-shaped surface fronts emerge due to abrupt changes in channel width associated with shoal regions (see Fig. B2). These fronts exhibit similar frontal dynamics and intense mixing, akin to the one near the constriction. In another region between the constriction and bend1, a surface convergence front forms as the flood current changes direction in the channel (Fig. B3). Note that this region includes a bridge located in the bottom right part of Fig. B3 at the easting distance of around −400 m, and the complex bathymetry attributed to anthropogenic influences may add to the variability in the salinity field.

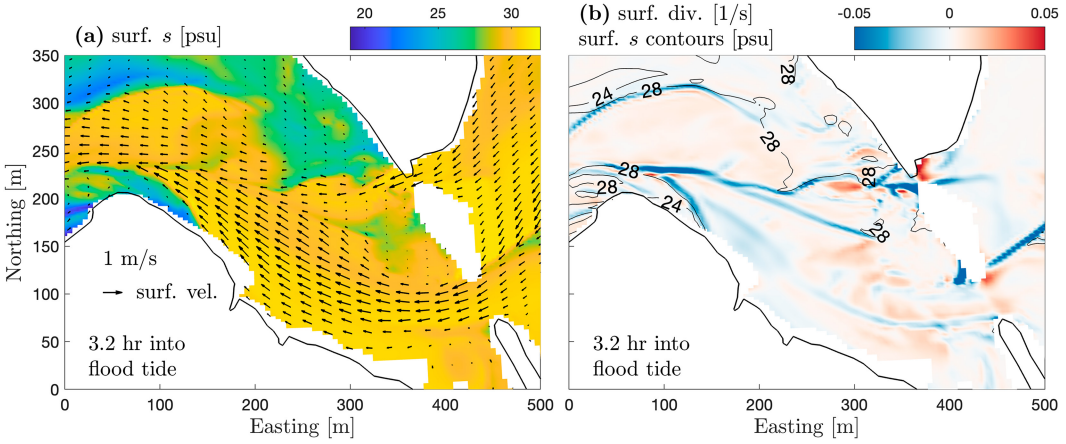

FIG. B1. The constriction region. (a) Surface salinity. Arrows show surface velocity. (b) Divergence of surface velocity, with blue colors representing surface convergence. This is the same region as Fig. 4, but at a later stage into the flood tide.

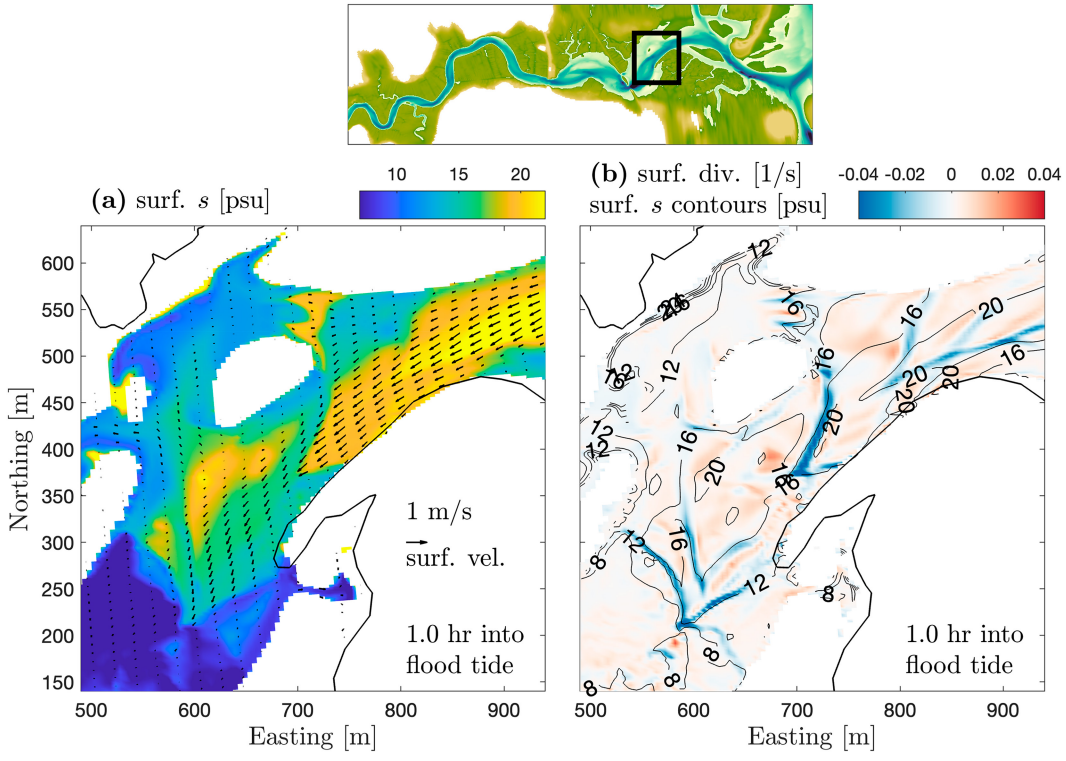

FIG. B2. A region between the estuary mouth and the constriction, at around 1.8 km from the mouth, corresponding to the rectangle in the bathymetric map. (a) Surface salinity. Arrows show surface velocity. (b) Divergence of surface velocity, with blue colors representing surface convergence.

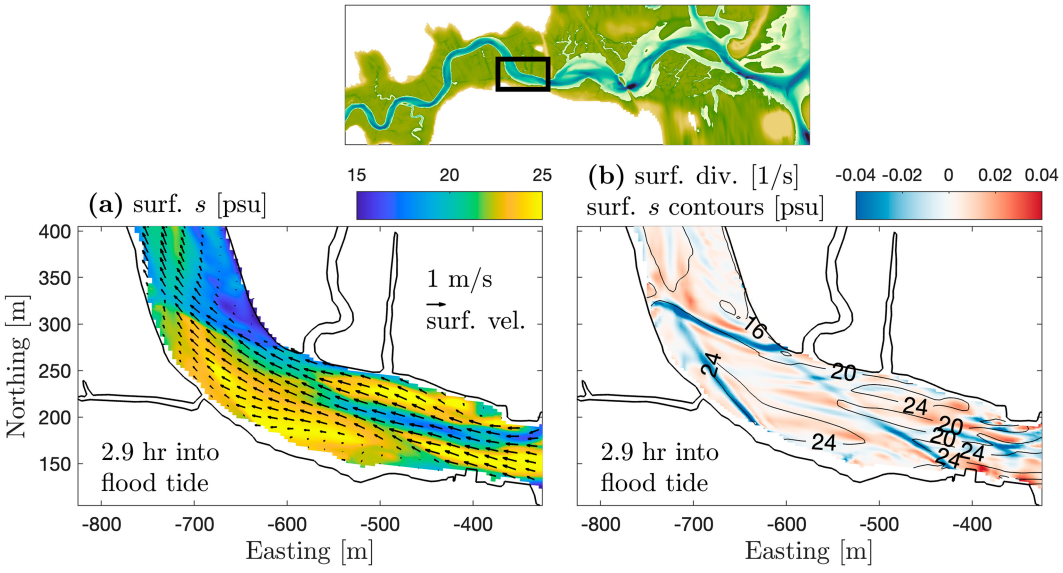

FIG. B3. A region between the constriction and bend1, at around 3 km from the estuary mouth, corresponding to the rectangle in the bathymetric map. (a) Surface salinity. Arrows show surface velocity. (b) Divergence of surface velocity, with blue colors representing surface convergence.

REFERENCES

Armi, L., and D. M. Farmer, 1986: Maximal two-layer exchange through a contraction with barotropic net flow. *J. Fluid Mech.*, **164**, 27–51, https://doi.org/10.1017/S0022112086002458.

Becherer, J., M. T. Stacey, L. Umlauf, and H. Burchard, 2015: Lateral circulation generates flood tide stratification and estuarine exchange flow in a curved tidal inlet. *J. Phys. Oceanogr.*, **45**, 638–656, https://doi.org/10.1175/JPO-D-14-0001.1.

Blanckaert, K., 2015: Flow separation at convex banks in open channels. *J. Fluid Mech.*, **779**, 432–467, https://doi.org/10.1017/jfm.2015.397.

Bo, T., and D. K. Ralston, 2020: Flow separation and increased drag coefficient in estuarine channels with curvature. *J. Geophys. Res. Oceans*, **125**, e2020JC016267, https://doi.org/10.1029/2020JC016267.

——, and ——, 2022: Frontogenesis, mixing, and stratification in estuarine channels with curvature. *J. Phys. Oceanogr.*, **52**, 1333–1350, https://doi.org/10.1175/JPO-D-21-0298.1.

——, ——, W. M. Kranenburg, W. R. Geyer, and P. Traykovski, 2021: High and variable drag in a sinuous estuary with intermittent stratification. *J. Geophys. Res. Oceans*, **126**, e2021JC017327, https://doi.org/10.1029/2021JC017327.

——, ——, and W. R. Geyer, 2023: Sources of drag in estuarine meanders: Momentum redistribution, bottom stress enhancement, and bend-scale form drag. *J. Phys. Oceanogr.*, **53**, 1629–1650, https://doi.org/10.1175/JPO-D-22-0211.1.

Brown, J., W. R. Turrell, and J. H. Simpson, 1991: Aerial surveys of axial convergent fronts in UK estuaries and the implications for pollution. *Mar. Pollut. Bull.*, **22**, 397–400, https://doi.org/10.1016/0025-326X(91)90343-Q.

Burchard, H., and H. Rennau, 2008: Comparative quantification of physically and numerically induced mixing in ocean models. *Ocean Modell.*, **20**, 293–311, https://doi.org/10.1016/j.ocemod.2007.10.003.

Chant, R. J., and R. E. Wilson, 1997: Secondary circulation in a highly stratified estuary. *J. Geophys. Res.*, **102**, 23 207–23 215, https://doi.org/10.1029/97JC00685.

Collignon, A. G., and M. T. Stacey, 2012: Intratidal dynamics of fronts and lateral circulation at the shoal–channel interface in a partially stratified estuary. *J. Phys. Oceanogr.*, **42**, 869–883, https://doi.org/10.1175/JPO-D-11-065.1.

——, and ——, 2013: Turbulence dynamics at the shoal–channel interface in a partially stratified estuary. *J. Phys. Oceanogr.*, **43**, 970–989, https://doi.org/10.1175/JPO-D-12-0115.1.

Dietrich, W. E., and J. D. Smith, 1983: Influence of the point bar on flow through curved channels. *Water Resour. Res.*, **19**, 1173–1192, https://doi.org/10.1029/WR019i005p01173.

Garcia, A. M. P., W. R. Geyer, and N. Randall, 2022: Exchange flows in tributary creeks enhance dispersion by tidal trapping. *Estuaries Coasts*, **45**, 363–381, https://doi.org/10.1007/s12237-021-00969-4.

Garvine, R. W., 1974: Dynamics of small-scale oceanic fronts. *J. Phys. Oceanogr.*, **4**, 557–569, https://doi.org/10.1175/1520-0485(1974)004<0557:DOSSOF>2.0.CO;2.

Geyer, W. R., 1993: Three-dimensional tidal flow around headlands. *J. Geophys. Res.*, **98**, 955–966, https://doi.org/10.1029/92JC02270.

——, and D. K. Ralston, 2015: Estuarine frontogenesis. *J. Phys. Oceanogr.*, **45**, 546–561, https://doi.org/10.1175/JPO-D-14-0082.1.

——, J. H. Trowbridge, and M. M. Bowen, 2000: The dynamics of a partially mixed estuary. *J. Phys. Oceanogr.*, **30**, 2035–2048, https://doi.org/10.1175/1520-0485(2000)030<2035:TDOAPM>2.0.CO;2.

——, D. K. Ralston, and R. C. Holleman, 2017: Hydraulics and mixing in a laterally divergent channel of a highly stratified estuary. *J. Geophys. Res. Oceans*, **122**, 4743–4760, https://doi.org/10.1002/2016JC012455.

——, ——, and J.-L. Chen, 2020: Mechanisms of exchange flow in an estuary with a narrow, deep channel and wide, shallow shoals. *J. Geophys. Res. Oceans*, **125**, e2020JC016092, https://doi.org/10.1029/2020JC016092.

Giddings, S. N., and Coauthors, 2012: Frontogenesis and frontal progression of a trapping-generated estuarine convergence front and its influence on mixing and stratification. *Estuaries Coasts*, **35**, 665–681, https://doi.org/10.1007/s12237-011-9453-z.

Haidvogel, D. B., and Coauthors, 2008: Ocean forecasting in terrain-following coordinates: Formulation and skill assessment of the regional ocean modeling system. *J. Comput. Phys.*, **227**, 3595–3624, https://doi.org/10.1016/j.jcp.2007.06.016.

Howard, L. N., 1961: Note on a paper of John W. Miles. *J. Fluid Mech.*, **10**, 509–512, https://doi.org/10.1017/S0022112061000317.

Huguenard, K. D., A. Valle-Levinson, M. Li, R. J. Chant, and A. J. Souza, 2015: Linkage between lateral circulation and near-surface vertical mixing in a coastal plain estuary. *J. Geophys. Res. Oceans*, **120**, 4048–4067, https://doi.org/10.1002/2014JC010679.

Kalkwijk, J. P. T., and R. Booij, 1986: Adaptation of secondary flow in nearly-horizontal flow. *J. Hydraul. Res.*, **24**, 19–37, https://doi.org/10.1080/00221688609499330.

Kalra, T. S., X. Li, J. C. Warner, W. R. Geyer, and H. Wu, 2019: Comparison of physical to numerical mixing with different tracer advection schemes in estuarine environments. *J. Mar. Sci. Eng.*, **7**, 338, https://doi.org/10.3390/jmse7100338.

Kranenburg, W. M., W. R. Geyer, A. M. P. Garcia, and D. K. Ralston, 2019: Reversed lateral circulation in a sharp estuarine bend with weak stratification. *J. Phys. Oceanogr.*, **49**, 1619–1637, https://doi.org/10.1175/JPO-D-18-0175.1.

Lacy, J. R., and S. G. Monismith, 2001: Secondary currents in a curved, stratified, estuarine channel. *J. Geophys. Res.*, **106**, 31 283–31 302, https://doi.org/10.1029/2000JC000606.

——, M. T. Stacey, J. R. Burau, and S. G. Monismith, 2003: Interaction of lateral baroclinic forcing and turbulence in an estuary. *J. Geophys. Res.*, **108**, 3089, https://doi.org/10.1029/2002JC001392.

Largier, J. L., 1992: Tidal intrusion fronts. *Estuaries*, **15**, 26–39, https://doi.org/10.2307/1352707.

——, 1993: Estuarine fronts: How important are they? *Estuaries*, **16** (1), 1–11, https://doi.org/10.2307/1352760.

Leeder, M. R., and P. H. Bridges, 1975: Flow separation in meander bends. *Nature*, **253**, 338–339, https://doi.org/10.1038/253338a0.

Leopold, L. B., and M. G. Wolman, 1960: River meanders. *Geol. Soc. Amer. Bull.*, **71**, 769–793, https://doi.org/10.1130/0016-7606(1960)71[769:RM]2.0.CO;2.

Lerczak, J. A., and W. R. Geyer, 2004: Modeling the lateral circulation in straight, stratified estuaries. *J. Phys. Oceanogr.*, **34**, 1410–1428, https://doi.org/10.1175/1520-0485(2004)034<1410:MTLCIS>2.0.CO;2.

Li, M., P. Cheng, R. Chant, A. Valle-Levinson, and K. Arnott, 2014: Analysis of vortex dynamics of lateral circulation in a straight tidal estuary. *J. Phys. Oceanogr.*, **44**, 2779–2795, https://doi.org/10.1175/JPO-D-13-0212.1.

Li, X., W. R. Geyer, J. Zhu, and H. Wu, 2018: The transformation of salinity variance: A new approach to quantifying the influence of straining and mixing on estuarine stratification. *J. Phys. Oceanogr.*, **48**, 607–623, https://doi.org/10.1175/JPO-D-17-0189.1.

Luettich, R. A., and Coauthors, 1992: ADCIRC: An advanced three-dimensional circulation model for shelves, coasts, and estuaries. Report 1, Theory and methodology of ADCIRC-2DD1 and ADCIRC-3DL. Dredging Research Program Tech. Rep. DRP-92-6, 146 pp., https://adcirc.org/wp-content/uploads/sites/2255/2018/11/1992_Luettich02.pdf.

MacDonald, D. G., and W. R. Geyer, 2005: Hydraulic control of a highly stratified estuarine front. *J. Phys. Oceanogr.*, **35**, 374–387, https://doi.org/10.1175/JPO-2692.1.

Marani, M., S. Lanzoni, D. Zandolin, G. Seminara, and A. Rinaldo, 2002: Tidal meanders. *Water Resour. Res.*, **38**, 1225, https://doi.org/10.1029/2001WR000404.

Marmorino, G. O., and C. L. Trump, 1996: High-resolution measurements made across a tidal intrusion front. *J. Geophys. Res.*, **101**, 25 661–25 674, https://doi.org/10.1029/96JC02384.

McWilliams, J. C., 2021: Oceanic frontogenesis. *Annu. Rev. Mar. Sci.*, **13**, 227–253, https://doi.org/10.1146/annurev-marine-032320-120725.

Miles, J. W., 1961: On the stability of heterogeneous shear flows. *J. Fluid Mech.*, **10**, 496–508, https://doi.org/10.1017/S0022112061000305.

Murphy, A. H., 1988: Skill scores based on the mean square error and their relationships to the correlation coefficient. *Mon. Wea. Rev.*, **116**, 2417–2424, https://doi.org/10.1175/1520-0493(1988)116<2417:SSBOTM>2.0.CO;2.

Nidzieko, N. J., J. L. Hench, and S. G. Monismith, 2009: Lateral circulation in well-mixed and stratified estuarine flows with curvature. *J. Phys. Oceanogr.*, **39**, 831–851, https://doi.org/10.1175/2008JPO4017.1.

Nunes, R. A., and J. H. Simpson, 1985: Axial convergence in a well-mixed estuary. *Estuarine Coastal Shelf Sci.*, **20**, 637–649, https://doi.org/10.1016/0272-7714(85)90112-X.

O'Donnell, J., 1993: Surface fronts in estuaries: A review. *Estuaries*, **16**, 12–39, https://doi.org/10.2307/1352761.

——, 1997: Observations of near-surface currents and hydrography in the Connecticut River plume with the surface current and density array. *J. Geophys. Res.*, **102**, 25 021–25 033, https://doi.org/10.1029/97JC01008.

Ralston, D. K., and M. T. Stacey, 2005: Longitudinal dispersion and lateral circulation in the intertidal zone. *J. Geophys. Res.*, **110**, C07015, https://doi.org/10.1029/2005JC002888.

——, G. W. Cowles, W. R. Geyer, and R. C. Holleman, 2017: Turbulent and numerical mixing in a salt wedge estuary: Dependence on grid resolution, bottom roughness, and turbulence closure. *J. Geophys. Res. Oceans*, **122**, 692–712, https://doi.org/10.1002/2016JC011738.

Scully, M. E., and W. R. Geyer, 2012: The role of advection, straining, and mixing on the tidal variability of estuarine stratification. *J. Phys. Oceanogr.*, **42**, 855–868, https://doi.org/10.1175/JPO-D-10-05010.1.

——, ——, and J. H. Trowbridge, 2011: The influence of stratification and nonlocal turbulent production on estuarine turbulence: An assessment of turbulence closure with field observations. *J. Phys. Oceanogr.*, **41**, 166–185, https://doi.org/10.1175/2010JPO4470.1.

Shchepetkin, A. F., and J. C. McWilliams, 2005: The Regional Oceanic Modeling System (ROMS): A split-explicit, free-surface, topography-following-coordinate oceanic model. *Ocean Modell.*, **9**, 347–404, https://doi.org/10.1016/j.ocemod.2004.08.002.

Simpson, J. E., and P. F. Linden, 1989: Frontogenesis in a fluid with horizontal density gradients. *J. Fluid Mech.*, **202**, 1–16, https://doi.org/10.1017/S0022112089001072.

Simpson, J. H., and R. A. Nunes, 1981: The tidal intrusion front: An estuarine convergence zone. *Estuarine Coastal Shelf Sci.*, **13**, 257–266, https://doi.org/10.1016/S0302-3524(81)80024-2.

——, and W. R. Turrell, 1986: Convergent fronts in the circulation of tidal estuaries. *Estuarine Variability*, D. A. Wolfe, Ed., Elsevier, 139–152, https://doi.org/10.1016/B978-0-12-761890-6.50013-7.

Stacey, M. T., and D. K. Ralston, 2005: The scaling and structure of the estuarine bottom boundary layer. *J. Phys. Oceanogr.*, **35**, 55–71, https://doi.org/10.1175/JPO-2672.1.

——, S. G. Monismith, and J. R. Burau, 1999: Observations of turbulence in a partially stratified estuary. *J. Phys. Oceanogr.*, **29**, 1950–1970, https://doi.org/10.1175/1520-0485(1999)029<1950:OOTIAP>2.0.CO;2.

Thomson, J., 1877: On the origin of windings of rivers in alluvial plains, with remarks on the flow of water round bends in pipes. *Proc. Roy. Soc. London*, **25**, 5–8, https://doi.org/10.1098/rspl.1876.0004.

Trowbridge, J. H., 1992: A simple description of the deepening and structure of a stably stratified flow driven by a surface stress. *J. Geophys. Res.*, **97**, 15 529–15 543, https://doi.org/10.1029/92JC01512.

Tyler, M. A., D. W. Coats, and D. M. Anderson, 1982: Encystment in a dynamic environment: Deposition of dinoflagellate cysts by a frontal convergence. *Mar. Ecol. Prog. Ser.*, **7**, 163–178, https://doi.org/10.3354/meps007163.

Umlauf, L., and H. Burchard, 2003: A generic length-scale equation for geophysical turbulence models. *J. Mar. Res.*, **61**, 235–265, https://doi.org/10.1357/002224003322005087.

Valle-Levinson, A., C. Li, K.-C. Wong, and K. M. M. Lwiza, 2000: Convergence of lateral flow along a coastal plain estuary. *J. Geophys. Res.*, **105**, 17 045–17 061, https://doi.org/10.1029/2000JC900025.

Wang, T., and Coauthors, 2022: Accumulation, transformation and transport of microplastics in estuarine fronts. *Nat. Rev. Earth Environ.*, **3**, 795–805, https://doi.org/10.1038/s43017-022-00349-x.

Warner, J. C., C. R. Sherwood, H. G. Arango, and R. P. Signell, 2005: Performance of four turbulence closure models implemented using a generic length scale method. *Ocean Modell.*, **8**, 81–113, https://doi.org/10.1016/j.ocemod.2003.12.003.

——, ——, R. P. Signell, C. K. Harris, and H. G. Arango, 2008: Development of a three-dimensional, regional, coupled wave, current, and sediment-transport model. *Comput. Geosci.*, **34**, 1284–1306, https://doi.org/10.1016/j.cageo.2008.02.012.

——, B. Armstrong, R. He, and J. B. Zambon, 2010: Development of a Coupled Ocean–Atmosphere–Wave–Sediment Transport (COAWST) modeling system. *Ocean Modell.*, **35**, 230–244, https://doi.org/10.1016/j.ocemod.2010.07.010.

——, Z. Defne, K. Haas, and H. G. Arango, 2013: A wetting and drying scheme for ROMS. *Comput. Geosci.*, **58**, 54–61, https://doi.org/10.1016/j.cageo.2013.05.004.

White, B. L., and K. R. Helfrich, 2013: Rapid gravitational adjustment of horizontal shear flows. *J. Fluid Mech.*, **721**, 86–117, https://doi.org/10.1017/jfm.2013.41.